Title

Online unsupervised detection of structural changes using train–induced dynamic responses

Authors

Meixedo, Andreia
Santos, João
Ribeiro, Diogo
et al.

Publication Date

2022-02-01

DOI

10.1016/j.ymssp.2021.108268

Peer reviewed

Online unsupervised detection of structural changes using train-induced dynamic responses

Andreia Meixedo[1], João Santos[2], Diogo Ribeiro[3], Rui Calçada[4], Michael D. Todd[5]

ABSTRACT

This paper exploits unsupervised data-driven structural health monitoring (SHM) in order to propose a continuous online procedure for damage detection based on train-induced dynamic bridge responses, taking advantage of the large-magnitude loading for enhancing sensitivity to small-scale structural changes. While such large responses induced by trains might create more damage-sensitive information in the measured response, it also amplifies the effects on those measurements from the environment. Thus, one of the biggest contributions herein is a methodology that exploits the large bridge responses induced by train passage while rejecting the confounding influences of the environment in such a way that false positive detections are mitigated. Furthermore, this research work introduces an adaptable confidence decision threshold that further improves damage detection over time. To ensure an online continuous assessment, a hybrid combination of autoregressive exogenous input (ARX) models, principal components analysis (PCA), and clustering algorithms was sequentially applied to the monitoring data, in a moving window process. A comparison between the performance obtained from autoregressive (AR) and ARX models as feature extractors was conducted, and it was concluded that ARX models lead to increased sensitivity to damage due to their ability to capture cross information between the sensors. The PCA proved its importance and effectiveness in removing observable changes induced by variations in train speed or temperature without the need to measure them, and the clustering methods allowed for an automatic classification of the damage-sensitive features. Since it was not possible to introduce damage to the bridge, several structural conditions were simulated with a highly reliable digital twin of the Sado Bridge, tuned with experimental data acquired from a SHM system installed on site, in order to test and validate the efficiency of the proposed procedure. The strategy proved to be robust when detecting a comprehensive set of damage scenarios with a false detection incidence of 2%. Moreover, it showed sensitivity to smaller damage levels (earlier in life), even when it consists of small stiffness reductions that do not impair structural safety and are imperceptible in the original signals.

Keywords: online assessment; unsupervised learning; damage detection; Structural Health Monitoring; traffic-induced dynamic responses; ARX model; PCA; cluster analysis.

[1] Ph.D. Student, CONSTRUCT-LESE, Faculty of Engineering, University of Porto, Portugal, ameixedo@fe.up.pt

[2] Researcher, LNEC, Laboratório Nacional de Engenharia Civil, Portugal, josantos@lnec.pt

[3] Adjunct Professor, CONSTRUCT-LESE, School of Engineering, Polytechnic of Porto, Portugal, drr@isep.ipp.pt

[4] Full Professor, CONSTRUCT-LESE, Faculty of Engineering, University of Porto, Portugal, ruiabc@fe.up.pt

[5] Full Professor, Department of Structural Engineering, University California San Diego, USA, mdtodd@eng.ucsd.edu

1. Introduction

The critical dependency of modern societies upon transport infrastructure such as roads or railway bridges and tunnels has motivated active research that aims to reduce the costs of inspection and maintenance. A large number of bridges are nearing the end of their original design life, and since this infrastructure cannot be economically replaced, techniques for damage detection are being developed and implemented so that their safe operation may be extended beyond the design basis for service life [1]. Structural health monitoring (SHM) represents a promising strategy in this ongoing challenge of achieving sustainable infrastructural systems since it has the potential to identify structural damage before it becomes critical, enabling early preventive actions to be taken to minimize costs [2]. The main goal of SHM should not be to replace the traditional inspection techniques, but to complement them with quantitative information [3,4]. Proactive conservation strategies based on long-term monitoring are increasingly recommended for special structures such as long-span bridges. In fact, disruption or even the collapse of a bridge can lead to important and irreversible negative consequences for society and the economy [5].

A combination of damage assessment technologies is necessary, and new developments in SHM aim at covering as many structures as possible at a reasonable cost. Although most bridges are already monitored using sophisticated measurement systems employing hundreds of sensors, there is a lack of useful and efficient interpretation of the results provided, with frequent difficulty in detecting early damage [6,7]. Thus, there is a need for data interpretation techniques that provide reliable information to assist engineers in structural management. It is crucial to devise robust online continuous SHM systems that allow structures to be designed and operated safely, without extended downtime periods associated with additional inspection or maintenance. Also, it is important to develop unsupervised data-driven SHM systems that can be used in any geometry and that can detect damage in old structures, which already have a changed structural condition, in order to support the decision making process related to maintenance and conservation strategies.

Damage identification techniques in civil engineering structures, including bridges, have consistently focused on ambient vibration or static responses. Modal-based damage-sensitive features are directly related to intrinsic parameters of the structure such as stiffness [8–11], which is expected to change in the presence of damage. In addition, modal quantities also have the advantage of being used for structural design and for assessing the vulnerability of the structures to actions and hazards [12]. Regardless of these advantages, ambient vibration analyses are typically based on small-magnitude responses that do not provide local damage-sensitive information or fail to excite nonlinearities where the damage might be more observable. Thus, Operational Modal Analysis (OMA)-based information can be considered insensitive to early damage due to the need of identifying high order modes shapes, which is particularly challenging for any real structure's complex loading combinations and environmental variability [13]. On the other hand, measuring static responses to generate health data cannot characterize the dynamic response, which often has its own unique and sensitive correlations to some kinds of damage. Recent works have been using the structural responses generated by traffic on bridges to take advantage of the repeatability of these actions, their known behaviour, and their great magnitude [14,15]. Azim & Gül [16] presented a sensor-clustering-based time-series analysis method for continuous global monitoring of girder-type railway bridges using operational data. The main limitations pointed out by the authors were the linear nature of the methods used and the influence of environmental condition changes, which was not considered in their study.

Moreover, the validation of the methodology was carried out with a numerical model that was not experimentally validated. Gonzalez & Karoumi [17] proposed a model-free damage detection method that uses deck accelerations and bridge weigh-in-motion data to train a machine learning setup based on ANN and a Gaussian process to classify the data into healthy or damaged. The method was further developed by Neves et al. [18], however, the limitations found for the proposed strategy were the limited number of damage scenarios and the non-consideration of environmental and operational effects. Nie et al. [19] proposed a data-driven damage detection method based on fixed moving principal component analysis to examine structural dynamic responses and monitor the damage occurrence. A beam bridge model subjected to stochastic loads was used in numerical simulation and experimental tests. The authors mentioned that further studies were necessary to determine the optimal number of sensors required for a reliable structural condition detection with respect to the sensor locations, structural types, size of structures, and quality of recorded data.

Despite the research made in this field, transient signals generated by traffic have not been used efficiently and robustly for damage detection. In the majority of the methodologies, their validation is performed using numerical simulations on simple structural elements, the type of damage studied is limited, the loading scenarios are very specific, the influence of environmental and operational variations (EOVs) on the structural response is often underestimated, and/or the online and unsupervised character is not fully addressed. All these constraints limit the usefulness of SHM for real complex bridges, especially in those where it is expected to be most useful, such as older and underperforming structures.

While the large dynamic responses induced by trains might create more damage-sensitive information in the measured response, it also amplifies the effects on those measurements from the environment. In this context, one of the biggest contributions herein is a machine learning procedure that exploits the large bridge responses induced by train passage while rejecting the confounding influences of the environment in such a way that false positive detections are mitigated. Furthermore, the unsupervised character of the proposed procedure includes the ability of detecting damage in bridges that already exhibit changed structural conditions, through an adaptable confidence decision threshold that further improves damage detection over time. This achievement plays a central role in the support to the decision making process related to maintenance and conservation strategies.

The proposed damage detection procedure aims at being generic enough to be applied to any type of railway bridges. The focus is placed on ensuring robustness and efficiency using a hybrid combination of autoregressive models with exogenous input (ARX) for feature extraction, principal component analysis (PCA) as well as Mahalanobis distance for feature modelling and data fusion, and cluster analysis for feature discrimination. The novelty lies in automatically extracting compact, meaningful information sets related to the bridge condition with a moving window data-driven strategy that allows a continuous and real-time damage detection with a negligible number of false positive detections. Finally, the use of a latent-variable method such as PCA grants the strategy the ability to remove EOVs without the need to measure them. The validation of the damage detection procedure is conducted using a highly reliable digital-twin of a complex long-span railway bridge along with experimental data as input, which proves its potential to be readily used on a real structure of interest.

It is worth noting that a different combination of techniques was firstly tested and presented in Meixedo et al. [20]. The machine learning strategy proposed herein is a clear step forward in terms of effectiveness, which allowed a completely online and automatic implementation.

2. The Sado Railway Bridge

2.1 Structure and monitoring system

The structural system studied herein is the bowstring arch bridge over the Sado River, located on the southern line of the Portuguese railway network that establishes the connection between Lisbon and Algarve (Figure 1). The structure is prepared for conventional and tilting passenger trains with speeds up to 250 km/h, as well as for freight trains with a maximum axle load of 25 t.

Figure 1. Overview of the Sado Bridge.

The bridge has a total length of 480 m, divided into 3 continuous spans each 160 m long, and it is part of a longer structure that includes the North access viaduct at 1115 m length and the South access viaduct with a length of 1140 m. As shown in Figure 2a, the bridge is suspended from three parabolic arches connected to each span of the deck by 18 hangers distributed over a single plane on the axis of the structure. The arches have a hexagonal hollow cross-section, with a variable width increasing towards the top. The bridge deck consists of a concrete slab laid over a U-shaped steel box girder. The connection between the deck and the hangers is performed through spherical hinges that allow the torsional rotation of the deck. The suspension of the deck loads is performed by the hangers by means of steel diaphragms and two diagonal strings at each connection. Each pier has a hexagonal hollow cross-section and rests on heads of reinforced concrete piles with lengths up to 50 m and 2 m diameters. Piers P1 and P4 are supported by nine piles, while piers P2 and P3 by twelve. At the top of each pier, there are two spherical and multidirectional steel sliding bearing devices, 4 m apart. The bearing devices have a circular contact surface and include an antifriction layer in XLIDE material. The deck is fixed on pier P1 whereas on piers P2, P3 and P4 only the transverse movements of the deck are restrained.

The structural health of the railway bridge over the Sado River has been monitored with a comprehensive autonomous online monitoring system (Figure 2) since the beginning of its life cycle. To identify each train that crosses the bridge and compute its speed, two pairs of optical sensors were installed at both ends of the bridge. The structural temperature action is measured by twelve NTC thermistors installed in three sections of the arch, four NTC thermistors fixed to the steel box girder and three PT100 sensors embedded in the concrete slab. To control the behaviour of the bearing devices, one longitudinal MEMS DC accelerometer was installed on top of each pier. The set of sensors also includes one vertical piezoelectric accelerometer fixed at the mid-span of the concrete slab, two triaxial force balance accelerometers at the thirds of the mid-span steel box girder and twelve vertical force balance accelerometers fixed along each span of the steel box girder. Data acquisition is carried out continuously by a locally deployed industrial computer in order to save the time history while the train is crossing. The responses of the optical sensors are acquired at a sampling rate of 2000 Hz, while the responses of the remaining sensors are acquired at 200 Hz.

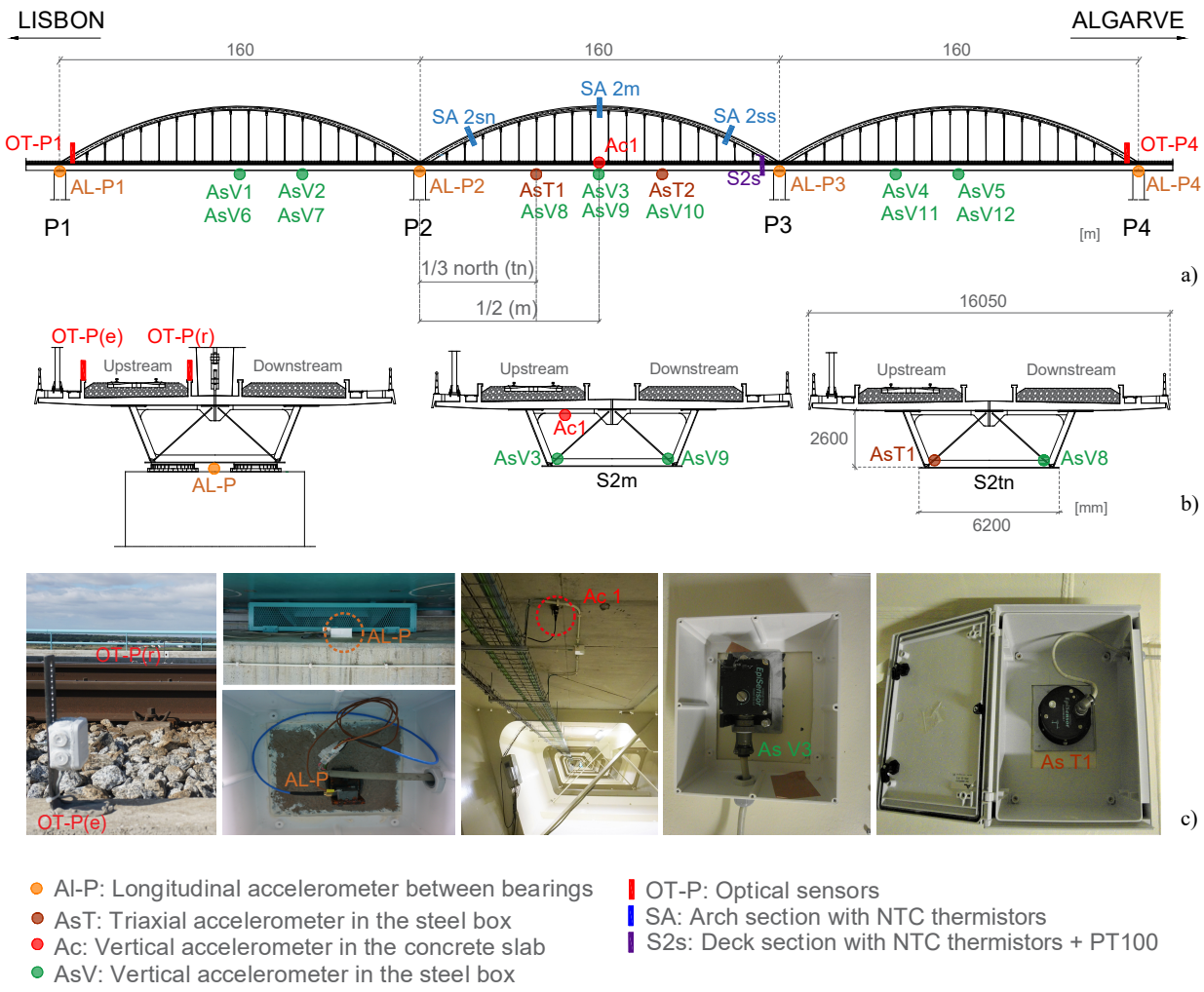

Figure 2. SHM system installed in the Sado railway bridge: a) overview, b) cross-section of the deck with the sensors location, c) photographs of the sensors installed in situ.

2.2 Dynamic numerical simulation

To test the machine learning strategy proposed in Section 3 and the online damage detection procedure described in Section 4, the monitored structural response of the Sado railway bridge was replicated using dynamic numerical simulations comprising realistic damage scenarios, since it was not possible to obtain such conditions experimentally. For this purpose, a 3D numerical model (Figure 3) composed of 38620 finite elements was developed in the ANSYS software [21] and validated using experimental measurements. Among the modelled structural elements, those defined as beam finite elements consist of piers, sleepers, ballast-retaining walls, rails, arches, hangers, transverse stiffeners, diaphragms, and diagonals. Shell elements were used to model the concrete slab and the steel box girder, while the rail pads, the ballast layer and the foundations were modelled using linear spring-dashpot assemblies. The mass of the non-structural elements and the ballast layer was distributed along the concrete slab. Concentrated mass elements were used to reproduce the mass of the arches' diaphragms and the mass of the sleepers simply positioned at their extremities. The connection between the concrete slab and the upper flanges of the steel box girder, as well as the connection between the deck and the track, were performed using rigid links. A special focus was afforded to the bearing devices, since they can strongly influence the performance of the bridge. In order to simulate the sliding behaviour of the bearings, nonlinear contact elements were applied. These elements allow for contact and sliding between any pair of nodes and are capable of supporting compression forces normal to their plane and friction forces along the tangential directions based on

a Coulomb model. Their coefficient of friction μ was defined as 1.5% during the numerical analysis, based on the design specifications [22]. Additionally, constraint elements located between the bearings were used to restrict the transversal movement in each pier, and both longitudinal and transversal movements in the case of the first pier.

The deck's steel was defined with a modulus of elasticity of 210 GPa, a Poisson's ratio of 0.3 and a density of 7850 kg/m^3, while the concrete slab and piers have a density of 2500 kg/m^3, a Poisson's ratio of 0.15 and a modulus of elasticity of 43 GPa based on the updated model presented in [23]. The boundary conditions were simulated using the results obtained from in-situ geotechnical tests conducted during the construction of the bridge [22]. An equivalent soil stiffness in each direction was computed and included in the numerical model of the bridge using spring elements. During these calculations, the SPT N-values and the shear wave velocity of the soil (Vs), obtained from the in-situ tests, were considered, along with the classification of the soil resulting from the laboratory analyses of the samples collected during the same tests.

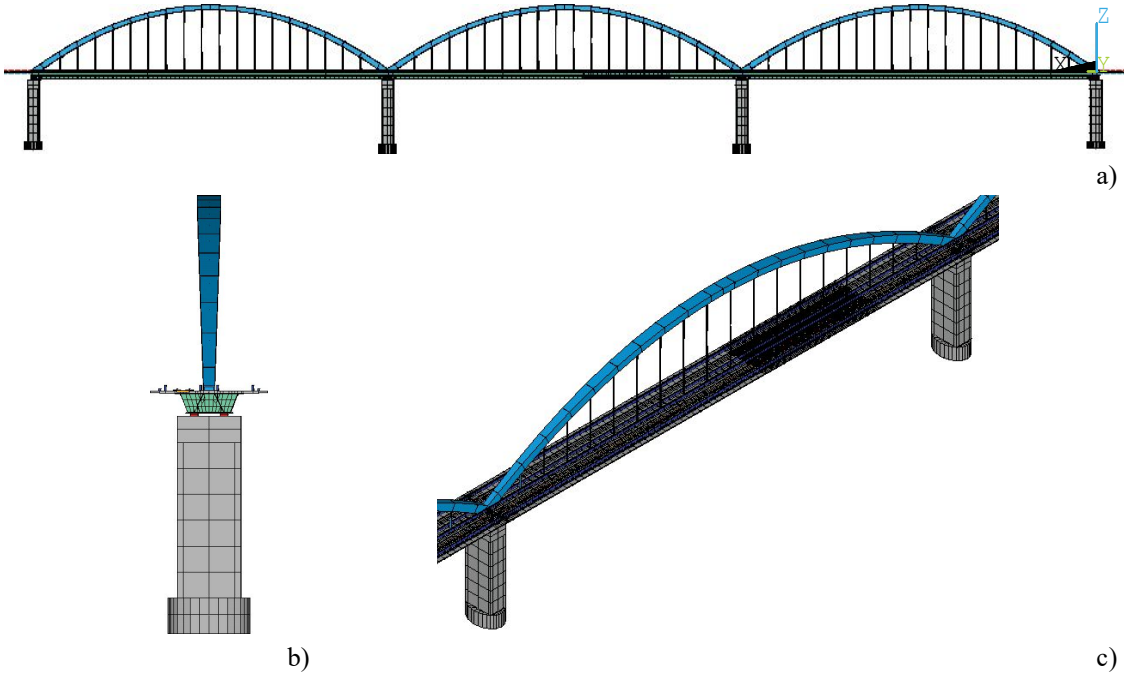

Figure 3. 3D numerical model of the railway Sado bridge: a) lateral view, b) front view, and c) middle span detail.

The dynamic numerical simulations conducted in the present work followed the aim of reproducing the structural quantities being measured, at the exact locations of the actual sensors installed on site, as a train crosses the bridge. To accurately replicate these structural responses, the temperature action measured by the SHM system precisely during each train crossing was introduced as input in the numerical model. A clustering strategy was considered regarding the input of the experimentally acquired temperatures in the numerical elements. The steel box was divided into four clusters, the concrete slab was divided into three, and each arch was also divided into three clusters, with the temperature being introduced in the upper and bottom part of the arch section. Using the measurements of the optical sensor network installed at both ends of the bridge, the train speed and axle configuration were obtained, and the train type was identified [24]. The dynamic analyses mentioned hereinafter were carried out for two of the passenger trains that normally cross the Sado Bridge, namely the Alfa Pendular (AP) train and the Intercity (IC) train. Their common speeds on the bridge are 220 km/h for the AP train and 190 km/h for the IC train. The loading schemes of both trains are presented in Figure 4. Rayleigh damping was

used with the damping matrix computed using the frequencies and damping coefficients identified in an ambient vibration test performed on the structure [25]. The nonlinear problem was solved based on the full Newton-Raphson method and the dynamic analyses were performed by the Newmark direct integration method, using a moving loads methodology [26]. The integration time step used in the analyses was 0.005 s.

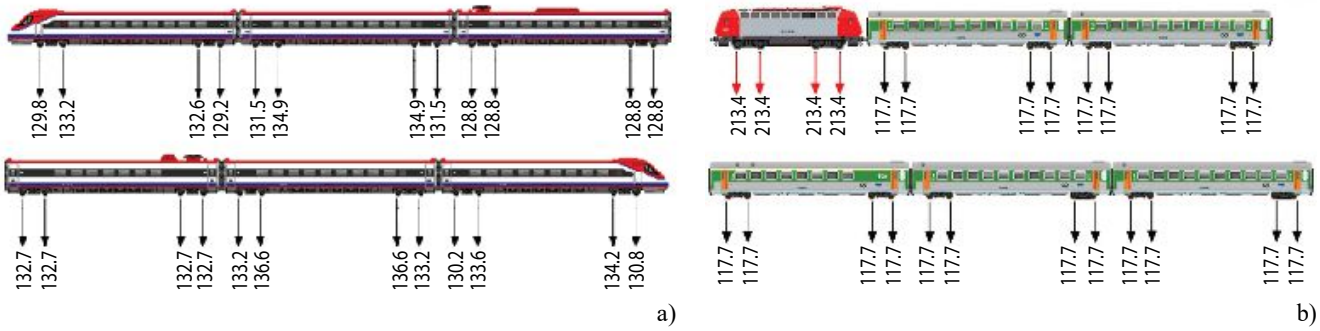

Figure 4. Trains and corresponding loading schemes: (a) Alfa Pendular, (b) Intercity.

To guarantee that the numerical model accurately simulates the structural behaviour of the bridge, the responses obtained from the dynamic analysis were compared with those measured by the SHM system (Figure 5). Numerical simulations were conducted considering the AP train as a set of moving loads crossing the Sado Bridge at a speed of 216 km/h. Figure 5a-c shows a very good agreement between experimental and numerical responses, in terms of longitudinal accelerations measured on pier P2 and vertical accelerations acquired on the concrete slab and on the steel box girder at the second mid-span. Regarding the auto-spectra resulting from the accelerations measurements, the main frequency is repeatedly 2.3 Hz, which corresponds to the passage of equally spaced axles groups of the AP train, illustrating a clear influence of the action on the bridge response. In Figure 5a, some frequencies around 10 Hz are not present in the numerical longitudinal accelerations. The corresponding modes may appear due to the action of seismic dampers that can be partially activated by rapid actions such as a train crossing. These elements were not modelled since they are extremely complex and in the majority of the cases are fully activated only during seismic events. Both experimental and numerical time-series are plotted as were acquired/simulated. They are synchronised, have a sampling rate of 200 Hz, and before the comparison were filtered based on a low-pass digital filter with a cut-off frequency equal to 15 Hz. A detailed description of the numerical modelling and its validation can be found in Meixedo et al. [27].

The structural response of the Sado Bridge during the passage of the AP and IC trains was replicated for the 23 accelerometers shown in Figure 2 using dynamic numerical simulations comprising several realistic scenarios, for both baseline and damaged conditions. Figure 6a summarizes different combinations for the baseline (undamaged) condition that aim at reproducing the bridge responses considering the variability of train type, speed, temperature actions, and loads. During each simulation, real temperatures measured by the SHM system were introduced in to the numerical elements. The average values for each season were 30ºC for summer, 16ºC for autumn, 10ºC for winter and 21ºC for spring, but the dispersion across the structure was considered by measuring and using temperature values in all elements of the bridge. The simulations included passages of the AP and IC trains (Figure 4), which were taken with ten different loading schemes, according to the experimental observations previously made by Pimentel et al. [28]. Three train speeds were considered for each type of train, as observed in Figure 6a, resulting in 100 dynamic simulations for the baseline condition, each taking approximately 10 hours of calculation time on a 4.2 GHz Quad-Core desktop with 32.0 GB of RAM.

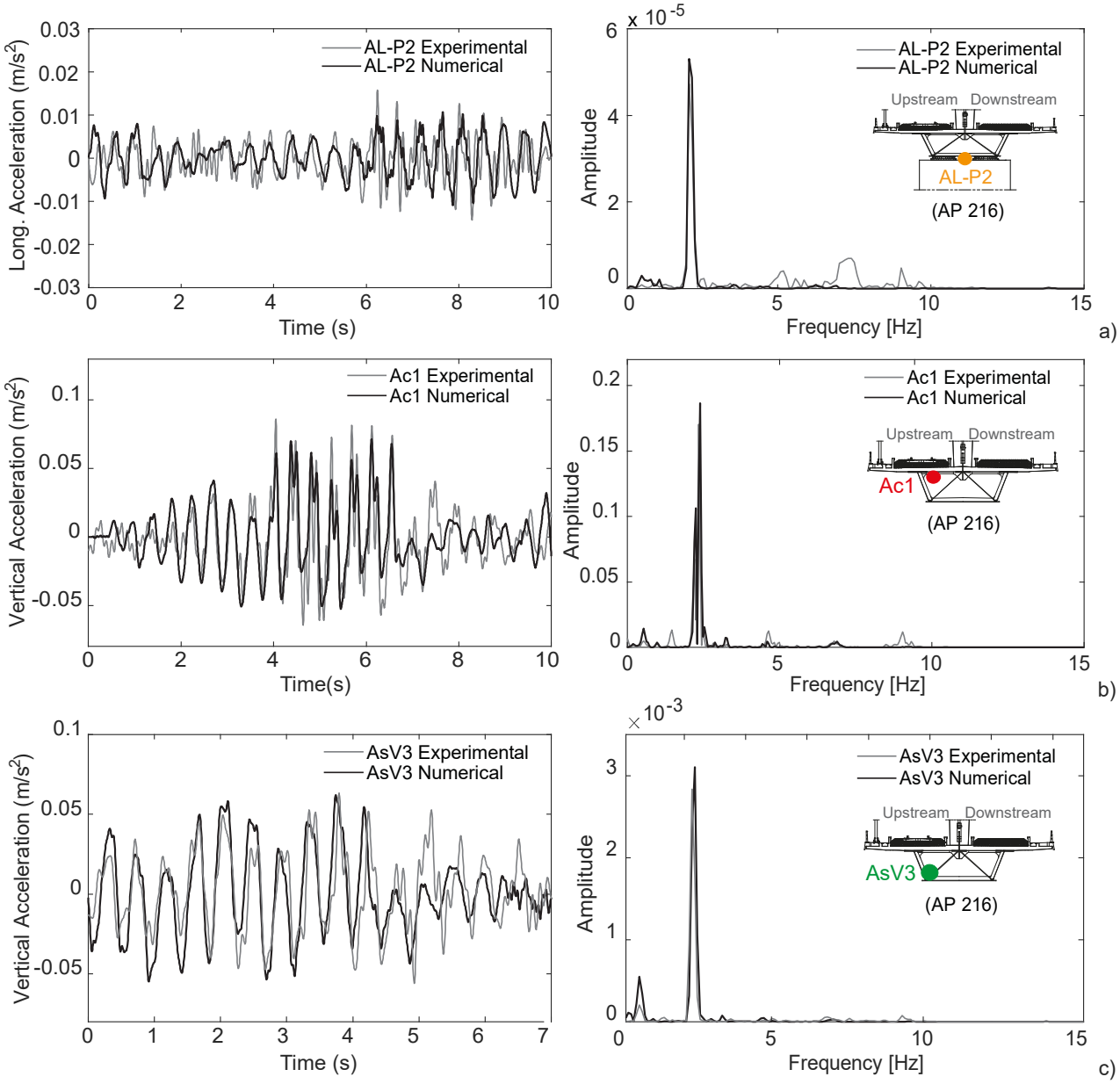

Figure 5. Numerical and experimental accelerations and corresponding auto-spectra, with the AP train crossing at 216 km/h: a) longitudinal accelerations at the pier (AL-P2), b) vertical accelerations at the concrete slab (Ac1), c) vertical accelerations at the steel box girder (AsV3).

The damage scenarios were chosen based on possible vulnerabilities identified for the type of structural system, taking into account its materials, connections, behaviour and loadings [29]. Among the several scenarios that can be considered, those related to friction increments in mechanical moving elements of the structural system (such as bearing devices), and those associated with corrosion in structural and reinforcing steel as well as cracking of concrete, were assumed as the most likely [29–32] and therefore simulated to validate the techniques presented herein. While friction increments were simulated in all bearing devices, cracking and corrosion were considered in several sections across the structure to ensure representativeness. Hence, damage scenarios were simulated, along with dynamic traffic loading, according to four different classes: i) damage in the bearing devices (type D1), ii) damage in the concrete slab (type D2), iii) damage in the diaphragms (type D3) and iv) damage in the arches (type D4). The locations of each type of damage are illustrated in Figure 6b, where different codes were assigned to each location depending on the damage type (e.g., D2:m1 is a damage in the concrete slab located in the first mid-span). Each scenario was simulated considering only one damage location. Regarding the

damages of type D1, it was simulated as a discrete damage and four severities were included, namely, increases of the friction coefficient from a reference value of 1.5% to 1.8%, 2.4%, 3.0% as well as to the full restraint of the movements between the pier and the deck. The remaining damage scenarios consisted of 5%, 10% and 20% stiffness reductions in the chosen sections of the bridge (Figure 6b). The damage type D2 consisted of a stiffness reduction in the cross section of the concrete slab comprising a 2 m length of the bridge and a damage-to-span length ratio of 1.25%. The damage type D3 involved a local stiffness reduction in one diaphragm. For each location of the damage type D4, a stiffness reduction was applied in an arch extension of 8 m, which represents 4.7% of the arc length. These structural changes were simulated by reducing the modulus of elasticity of the concrete (damage type D2) and of steel (damage types D3 and D4). Thus, a total of 114 damage scenarios were simulated for AP train crossings at 220 km/h, using the loading scheme presented in Figure 4a and adding as input the temperatures measured on site. Additional damage scenarios could have been simulated for different combinations of EOVs. However, as it will be discussed in section 3.2, the proposed methodology is effective in removing these effects and keeping only those generated by structural changes.

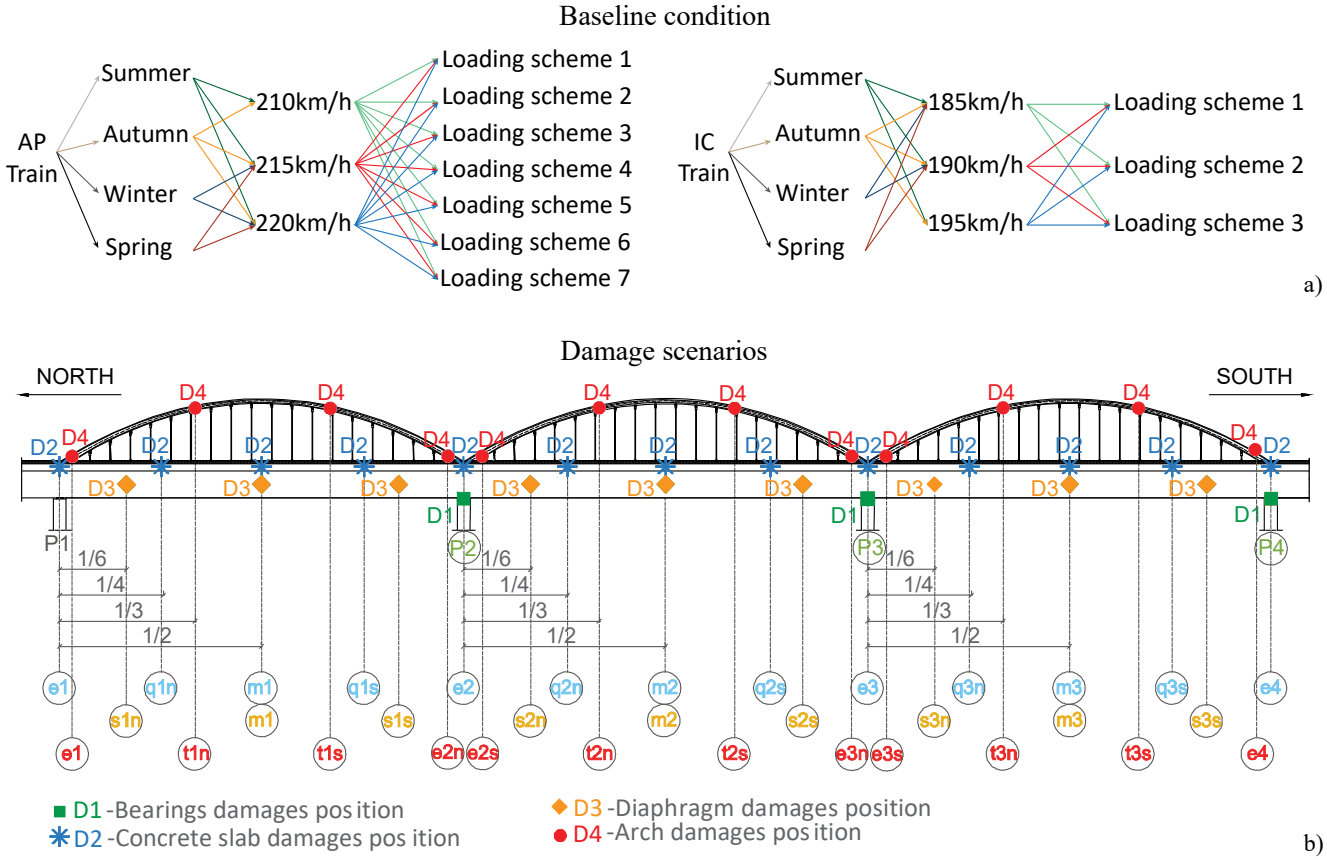

Figure 6. Baseline and damage scenarios: a) combination of simulations for the baseline condition, b) type and location of the damages.

To obtain the most similar and reliable reproduction of the real SHM data, the noise measured on site by each accelerometer was added to the corresponding numerical output. These noise distributions were acquired while no trains were travelling over the bridge on non-windy days. Each simulation was corrupted with different noise signals acquired at different days, thus ensuring the most representative validation for the techniques developed herein. Figure 7 presents an example of a vertical acceleration bridge response at the second mid-span of the concrete slab for an AP train crossing, before and after being corrupted. The noise distribution applied to the response, which was measured by sensor Ac1 of the SHM system, is also shown.

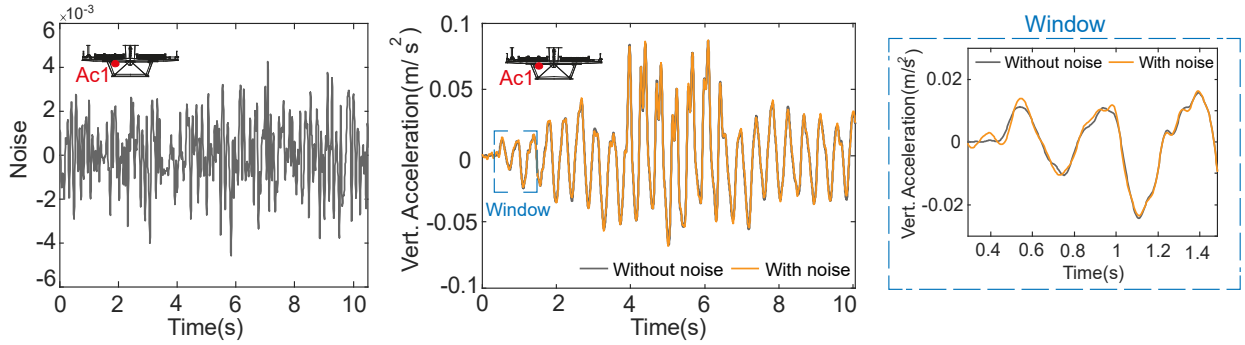

Figure 7. Experimental noise distribution and simulated vertical acceleration of the bridge before and after being corrupted.

The time-series illustrated in Figure 8 are examples of simulated responses for undamaged baseline conditions, acquired from the accelerometer located at the second mid-span of the concrete slab (Ac1). Each plot concerns a single event with variations associated to different train types, loading schemes, train speed and temperature actions. A clear distinction between the bridge responses to the crossings of the AP train (Figure 8a) and the IC train (Figure 8b) can be observed, showing the need of taking into account different train types for the development of damage detection strategies. Conversely, the same plots allow observing that different loading schemes generate smaller changes in the dynamic responses. This behaviour is expected since the trains considered are passenger trains, whereby the loading variation is small. Temperature action and train speed also influence the structural response imposed by trains crossing the bridge, as it can be readily observed in Figure 8c and Figure 8d for AP train crossings. Regarding Figure 8c, the specific combination between the autumn temperature and the train entering in the bridge leads to a more abrupt initial response of the structure in the first 2 seconds. Nevertheless, this frequency is quickly attenuated.

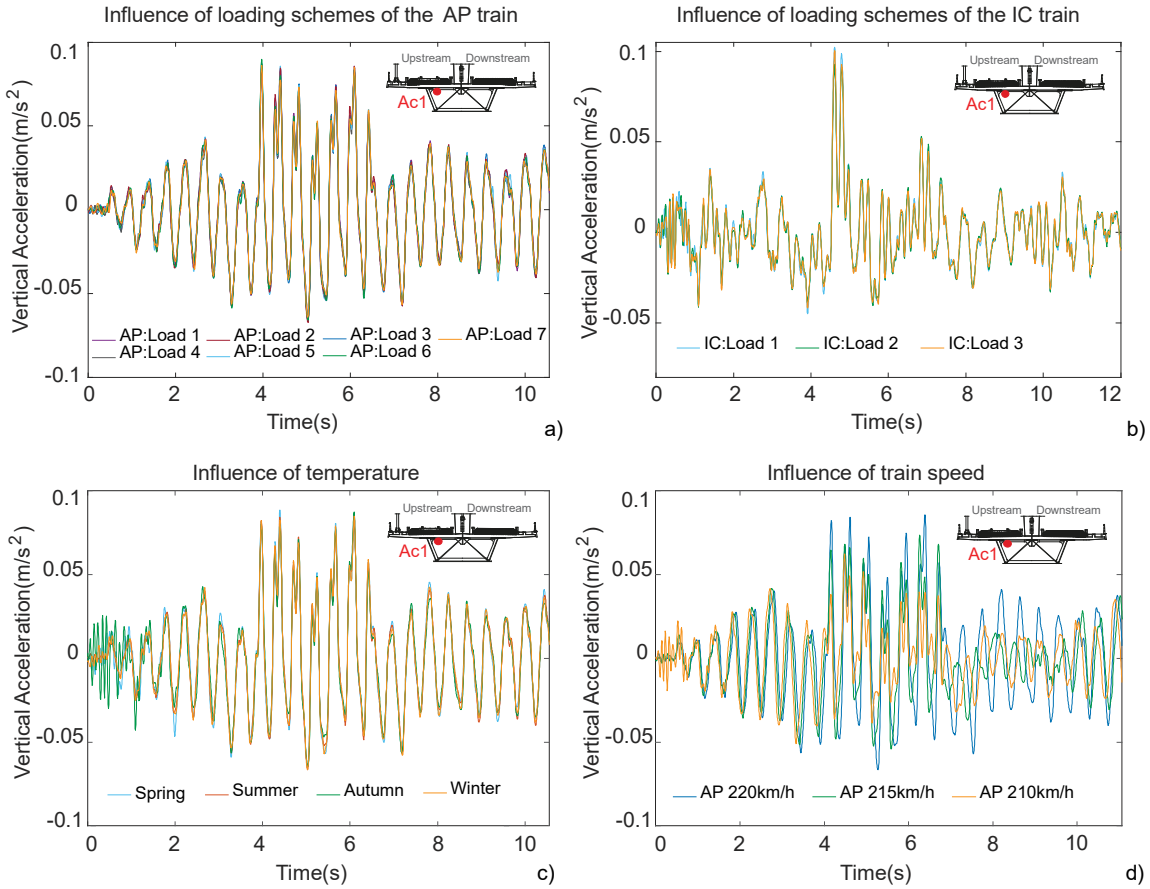

Figure 8. Baseline time-series simulations of sensor Ac1: a) using different loading schemes of the AP train at 220 km/h, b) using different loading schemes of the IC train at 190 km/h, c) using temperature measurements from different seasons, d) with the AP train traveling at different speeds.

Figure 9a,b shows examples of simulated responses of the Ac1 accelerometer for damaged scenarios in the concrete slab (D2: m2) and in the bearings on pier P2 (D1: P2), respectively, during a summer day and with the AP train crossing the bridge at 220 km/h. The influence of damage scenarios on the signal obtained for train crossings appears to be much smaller than that observed for changes in temperature actions, train type and train speed, even when analysing sensors adjacent to the damages and for the largest magnitudes considered (20% stiffness reduction and full restraint of the bearing). This conclusion can be easily derived from Figure 9, where the high overlapping of the time-series obtained from the baseline condition and the remaining ones puts in evidence the small magnitude of the simulated damage scenarios, which can be considered as early-damage.

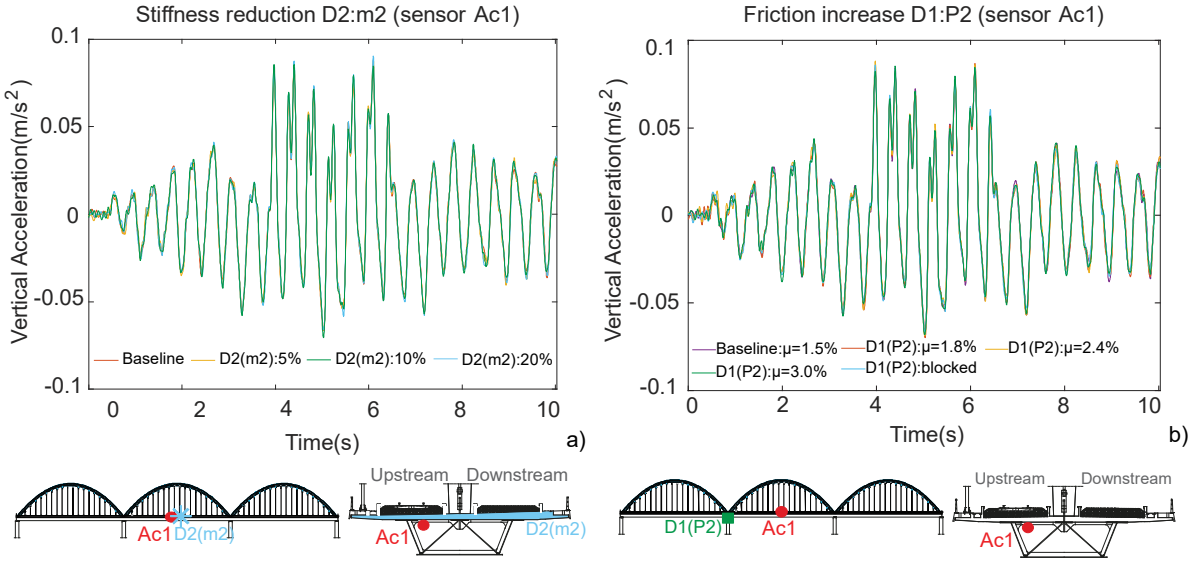

Figure 9. Time-series simulated for a summer day with the AP train at 220 km/h: a) stiffness reduction D2:m2 and vertical acceleration from sensor Ac1, b) friction increase D1:P2 and vertical acceleration from sensor Ac1.

3. Machine learning strategy for train-induced damage detection

3.1 Feature extraction

Features are extracted from a statistical time series analysis. In this section, a brief discussion about the autoregressive model with exogenous inputs (ARX) and the autoregressive (AR) model is presented. The ARX model regresses the current measurement upon finite measurements of its past and upon an exogenous input series:

$$y_j = \sum_{i=1}^{n_a} a_i y_{j-i} + \sum_{k=1}^{n_b} b_k x_{j-k} + \varepsilon_j \quad (1)$$

where y_j, x_j, and ε_j are output, input, and error terms of the model at the signal value j, respectively. On the other hand, n_a, n_b and a_i, b_k represent the orders and the parameters of the output and input data, respectively. The ARX model can be simplified to the AR model if n_b is set to zero:

$$y_j = \sum_{i=1}^{n_a} a_i y_{j-i} + \varepsilon_j \quad (2)$$

The process of extracting the AR/ARX parameters, a_i and b_k, is based on fitting the AR/ARX models to vibration time-domain responses, acquired from different sensors, in the undamaged and damaged conditions. The vectors of the AR/ARX model parameters in the baseline and damaged state conditions are used as the

damage-sensitive features, which depend on sensors from multiple locations. Typical time-series lead to an overdetermined set of equations that must be solved to obtain optimal estimates of the AR and ARX coefficients. There are several methods that can be used to solve the coefficients; the least-squares method was the one applied in this study [33].

Regarding the ARX model, the accelerometer located at the second mid-span of the concrete slab (Ac1 - Figure 2), named as the reference channel, was defined as output, y_j, since it is located in a central point of the bridge and is representative of its global behaviour. Each of the other installed sensors was defined as the input signal, x_j.

The ARX model orders should be rationally determined considering the data characteristics. Here, the Normalized Root Mean Square Error (NRMSE) fitness value (Eq. 3) was used to quantify the model accuracy according to the ARX order defined.

$$NRMSE = 1 - \frac{\sum_{i=1}^{n}(y_i - \hat{y}_i)^2}{\sum_{i=1}^{n}(y_i - \bar{y})^2} \tag{3}$$

where, y_i is the measured data, $\hat{y}_i$ is the simulated data through the ARX model, and $\bar{y}$ is the mean of the measured dataset. For each baseline structural condition, the parameters were estimated using the least squares technique applied to time-series from all twenty-three accelerometers, and the NRMSE values were computed for ARX models of increasing order. Figure 10 plots the average NRMSE values, which represent the difference between the actual data and the ARX model predicted data. It is possible to observe that the accuracy of the ARX model gradually increases with the ARX model order and appears to stabilize close to 30, whereby both the input and output orders of the ARX model were set to 30. The same output order was adopted for the AR model.

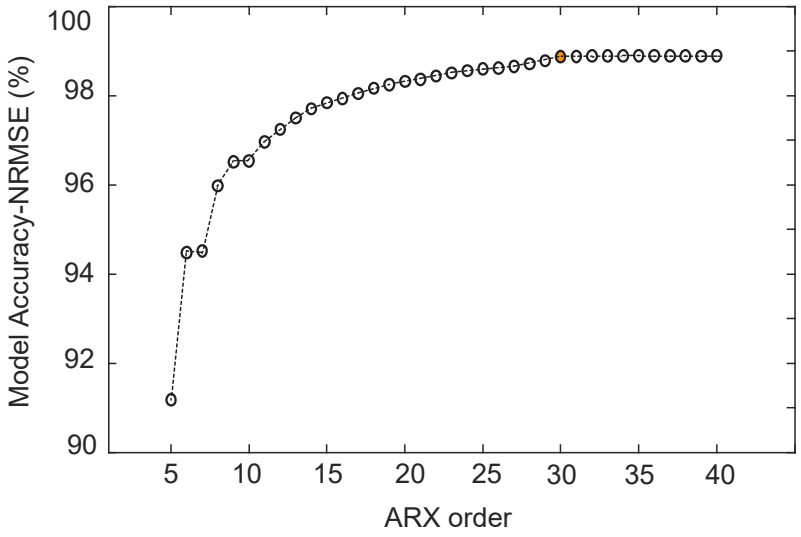

Figure 10. Model accuracy according to the ARX order.

Based on these assessments, for each structural condition and for each accelerometer, individual ARX (30, 30) and AR (30) models were implemented to fit the corresponding time-series and their parameters were used as damage-sensitive features.

Figure 11 shows the 60 ARX parameters for each of the 100 simulations of the baseline condition and 114 simulations of the damaged condition, considering as output the measurements from the accelerometer located at the second mid-span of the concrete slab (Ac1), and as input the measurements of the accelerometer located at

the second mid-span of the steel box girder (AsV3). A comparison of the features' amplitude between scenarios allows observing a higher variability of the ARX parameters for EOVs (Figure 11a) than for damages (Figure 11b). Additional damage-sensitive features were extracted likewise from each one of the remaining 21 accelerometers installed on site comprising time-series with 2112 measurements, which resulted in a three-dimensional feature matrix of *214-by-60-by-22* elements.

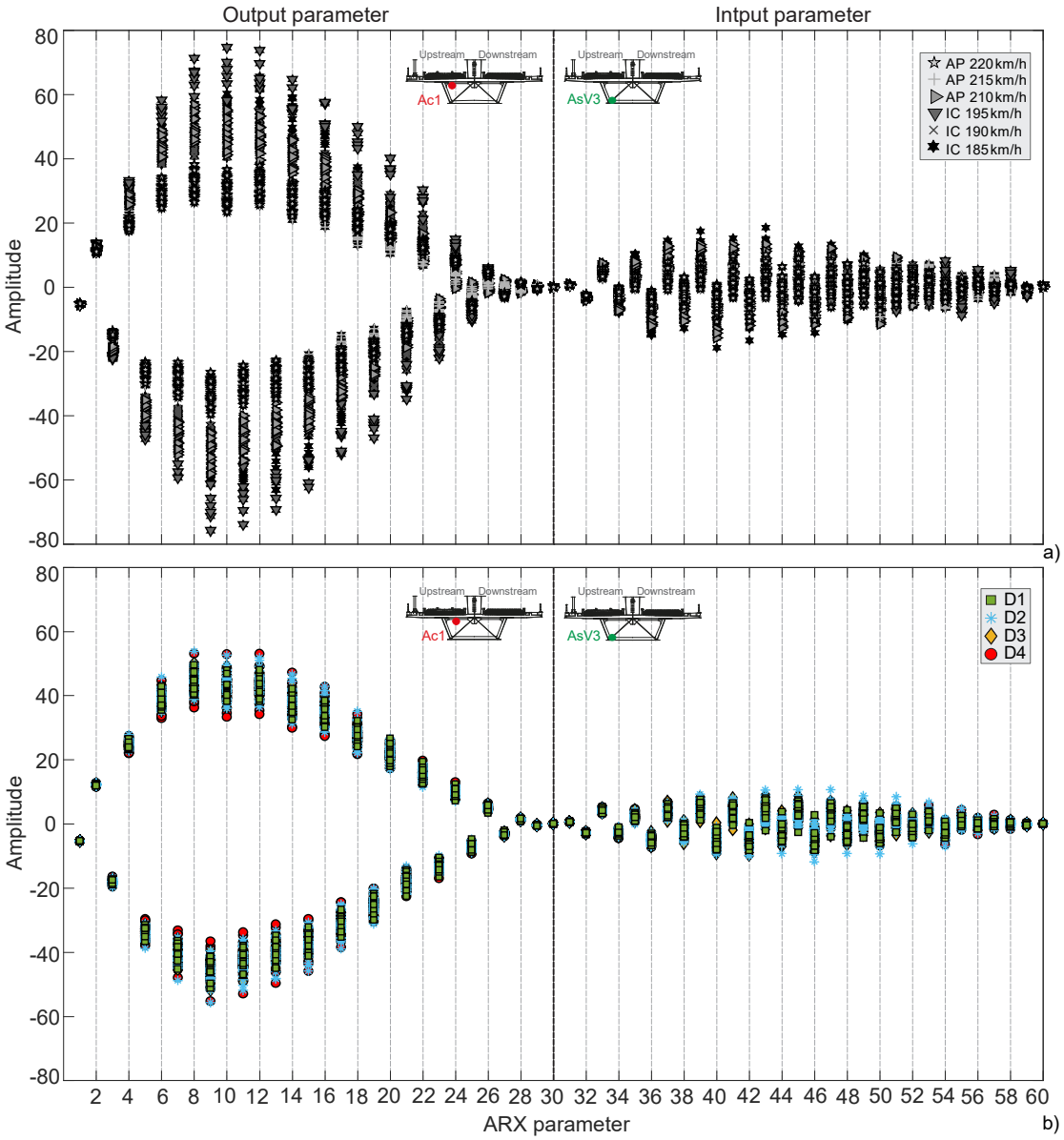

Figure 11. ARX features obtained from the simulated accelerations responses in the mid-span section of the concrete slab (Ac1) and steel-box girder (AsV3): a) for each of the 100 simulations of the baseline (undamaged) condition, b) for each of the 114 damage scenarios.

Figure 12 shows the 30 AR damage-sensitive features computed with the measurements from the accelerometer located at the second mid-span of the concrete slab (Ac1) for baseline and damaged conditions. As observed with the ARX parameters, comparing the undamaged (Figure 12a) and the damaged features (Figure 12b), the AR parameters also present a higher variability in the presence of a range of EOVs, compared to a range of damage scenarios. The outcome after applying the AR model to each structural condition and to each of the 23 accelerometers was a three-dimensional feature matrix of *214-by-30-by-23* elements.

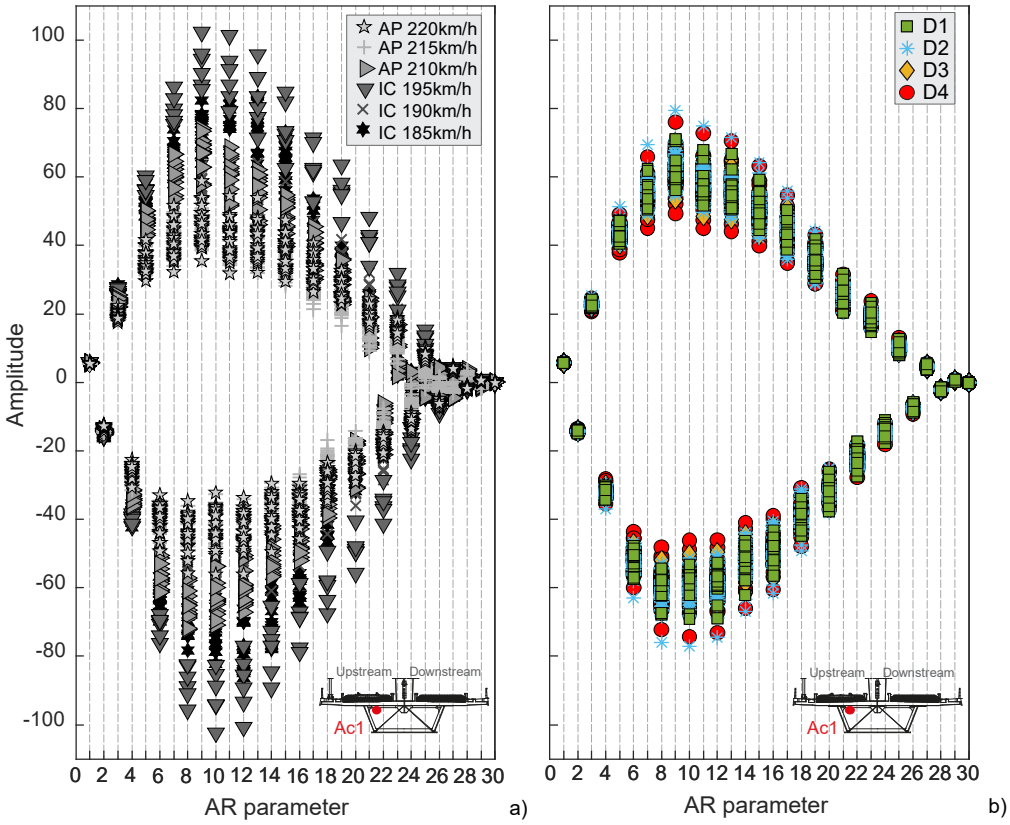

Figure 12. AR features obtained from the simulated accelerations responses in the mid-span section of the concrete slab (Ac1): a) for each of the 100 simulations of the baseline (undamaged) condition, b) for each of the 114 damage scenarios.

To illustrate the feature extraction procedure, Figure 13 details two ARX output parameters (ARX1 and ARX10) and two ARX input parameters (ARX50 and ARX60) obtained considering the output sensor Ac1 and the input sensor AsV3, as well as all the sixty ARX parameters (ARX1 to ARX60) represented by box-and-whisker plots. The features are divided into two major groups according to the structural condition: baseline (first 100 simulations) and damaged (114 subsequent simulations). In the plots shown in Figure 13a, for each baseline condition, the seven symbols in a row, in the case of the AP train, and the three symbols in a row, in the case of the IC train, represent the different loading schemes considered for each train type and speed, and for each temperature. For each damage location (codes from Figure 6), a sequence of three or four symbols represents different levels of severity (low to high from left to right).

A comparison between the values of the ARX1 and ARX10 output parameters across all 214 scenarios allows concluding that each feature is describing distinct trends of the analysed data. The main changes in the amplitudes of these parameters are induced by the type and speed of the train. In addition, for each value of speed, the observed changes in the amplitude of these parameters are generated by variations in the values of structural temperature (spanning all four seasonal average temperatures). The loading schemes are the operational factor with the least impact on the parameter variability in the baseline simulations. However, the input parameters ARX50 and ARX60 exhibit a completely different behaviour, since for them, the influence of EOVs (baseline) is not as predominant when compared to the influence of damage, as it is in the other two parameters (ARX1 and ARX10). Instead, the amplitude of the features has an identical magnitude in all 214 structural conditions. This trend can also be observed in the box-and-whisker plots presented in Figure 13b. For the output parameters (ARX1 to ARX30), there is an increased importance of the distributions of baseline conditions, and, consequently, of

EOVs, in relation to the distributions of damage scenarios, while, for the input parameters (ARX31 to ARX60) these distributions are more similar, which denotes an increase in the damage preponderance.

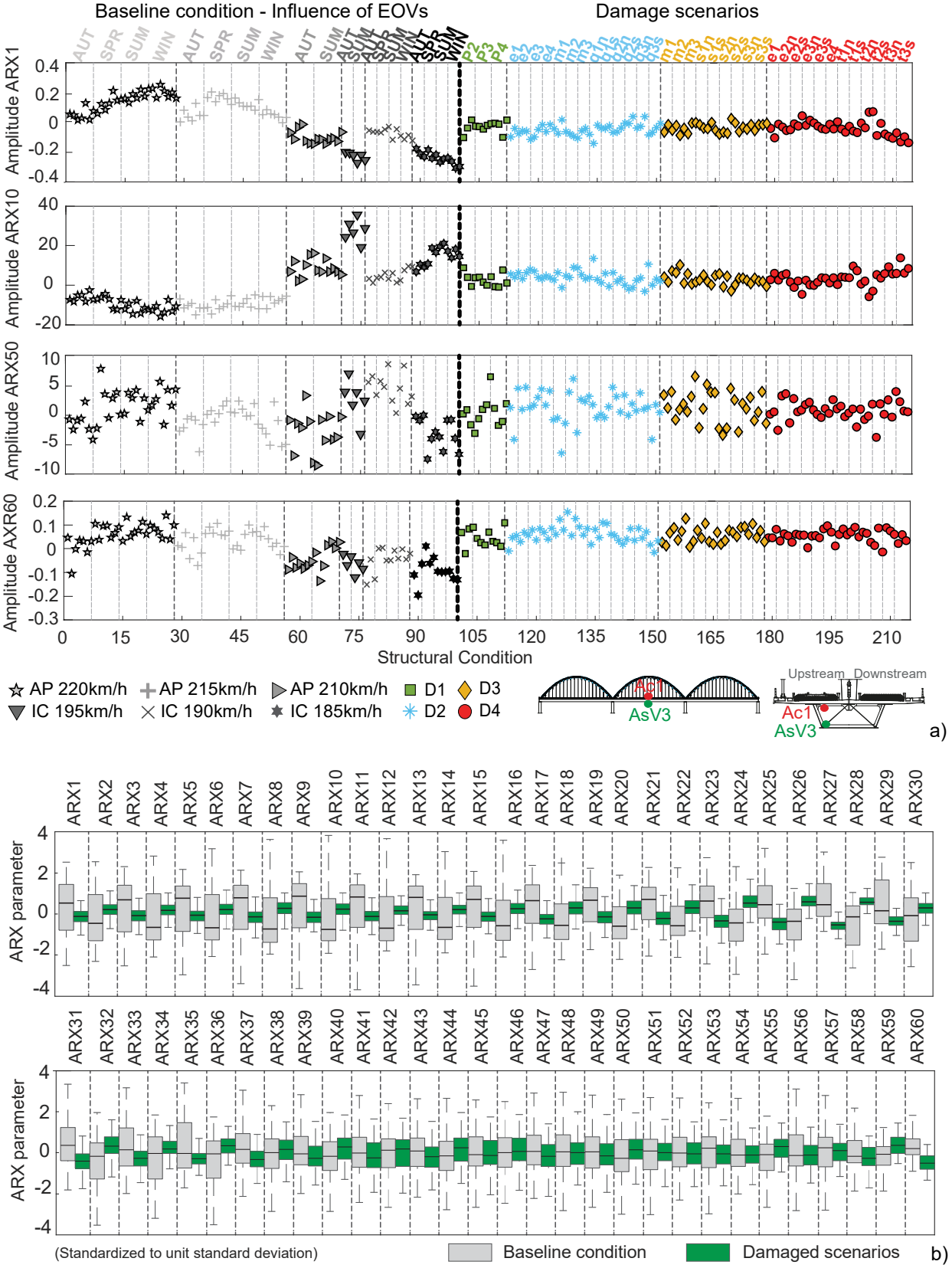

Figure 13. For all 214 structural conditions considering the simulated responses of accelerometer Ac1 as output and sensor AsV3 as input: a) amplitude of four of the sixty ARX parameters, b) box-and-whiskers plots representing the sixty ARX parameters.

The same study was also conducted for the thirty AR parameters obtained for sensor Ac1, with two of these (AR1 and AR10) shown in detail in Figure 14a. Here it is possible to observe that each feature is describing

distinct inner relationships of the analysed data and that the features from the baseline condition have a much higher amplitude variation than the features from damage scenarios. Figure 14b confirms that the distributions of all thirty AR parameters from damage scenarios vary significantly less when compared to the distributions of baseline conditions, which leads to a preponderance of EOVs, regardless of the type of damage as well as its location and severity.

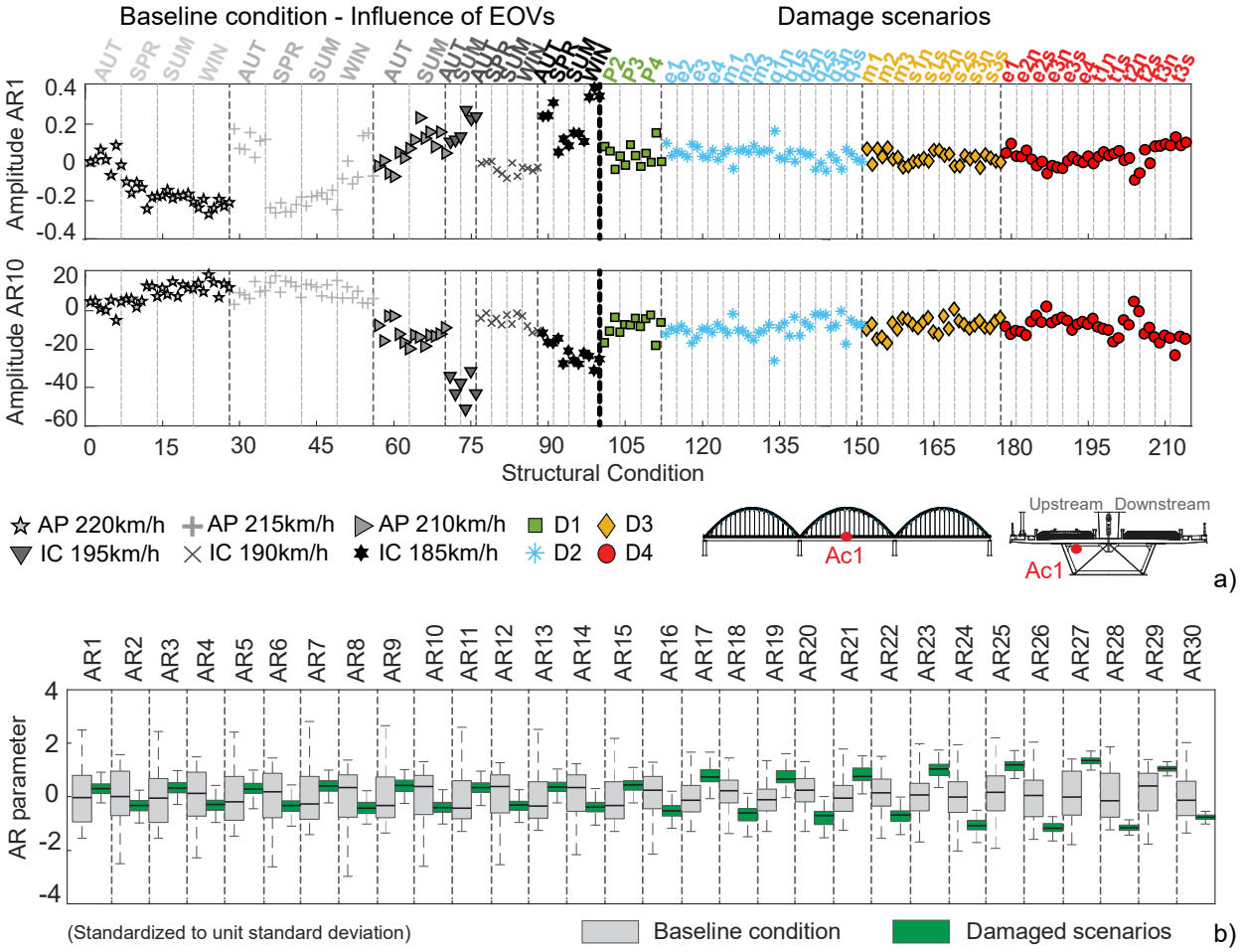

Figure 14. For all 214 structural conditions considering the simulated responses of accelerometer Ac1: a) amplitude of two of the thirty AR parameters, b) box-and-whiskers plots representing the thirty AR parameters.

The importance of a disperse sensors network can be observed in Figure 15, where the ARX features extracted for each state condition represent very distinct distributions depending on the input sensor. In this figure, the signal obtained from sensor Ac1 was taken as the output and each one of the sensors AsV3, AL-P3 and AsT_t2 as the input. Figure 15 illustrates the ARX features extracted for two simulations of the baseline condition: a) AP|220km/h|SUM: the AP train crossing the bridge at 220 km/h in a summer day, and b) AP|210km/h|AUT: the AP train at 210 km/h during an autumn day. The features extracted from the following four damage scenarios are also shown: a) D1 (P3: restrained), the full restraint of the bearing devices at pier P3, b) D2 (m2:20%), the 20% stiffness reduction in the second mid-span of the concrete slab, c) D3 (m2:20%), the 20% stiffness reduction at the diaphragm, also in the second mid-span, and d) D4 (t2s:20%), the 20% stiffness reduction in the arch at one-third south of the central span. The bar charts presented in Figure 15 were drawn from the sum of the differences between the amplitude of the parameters from each of these scenarios and the amplitude of the parameters from the baseline condition AP|220km/h|SUM.

The ARX parameters' amplitudes obtained from the output sensor Ac1 are higher than those extracted from the input sensors, especially for the damage scenario closest to this sensor - D2 (m2:20%). As expected,

comparing the bar charts of Figure 15a, b and c, there is a consistency in terms of the relative amplitude of the parameters from the output sensor Ac1, regardless of the input sensor. On the other hand, the features from sensor AsV3 have the lowest amplitude, which can be justified by the fact that this is the input sensor that is closest to the output sensor Ac1. The bar chart in Figure 15a shows that the ARX parameters from this input sensor are more sensitive to damage scenario D2 (m2:20%), which is adjacent to this sensor. Regarding the input sensor AL-P3 (Figure 15b), the features with the highest amplitude are those of the parameters of the damage scenario D1 (P3: restrained), which is also the closest to this sensor, as can be clearly confirmed in the bar chart of Figure 15b. This bar chart also shows the importance of considering and modelling EOVs, since the input parameters from the baseline condition AP|210km/h|AUT present an equal or higher relative amplitude than the damage scenarios D2, D3 and D4. Figure 15c presents the ARX input parameters extracted from sensor AsT_t2, which are highly sensitive to damage D1 (P3: restrained) and damage D2 (m2:20%). Its corresponding bar chart allows observing that, in this case, the ARX input parameters from the damage scenario D3 (m2:20%) and the baseline scenario AP|210km/h|AUT have less sensitivity than those extracted from the baseline scenario AP|220km/h|SUM.

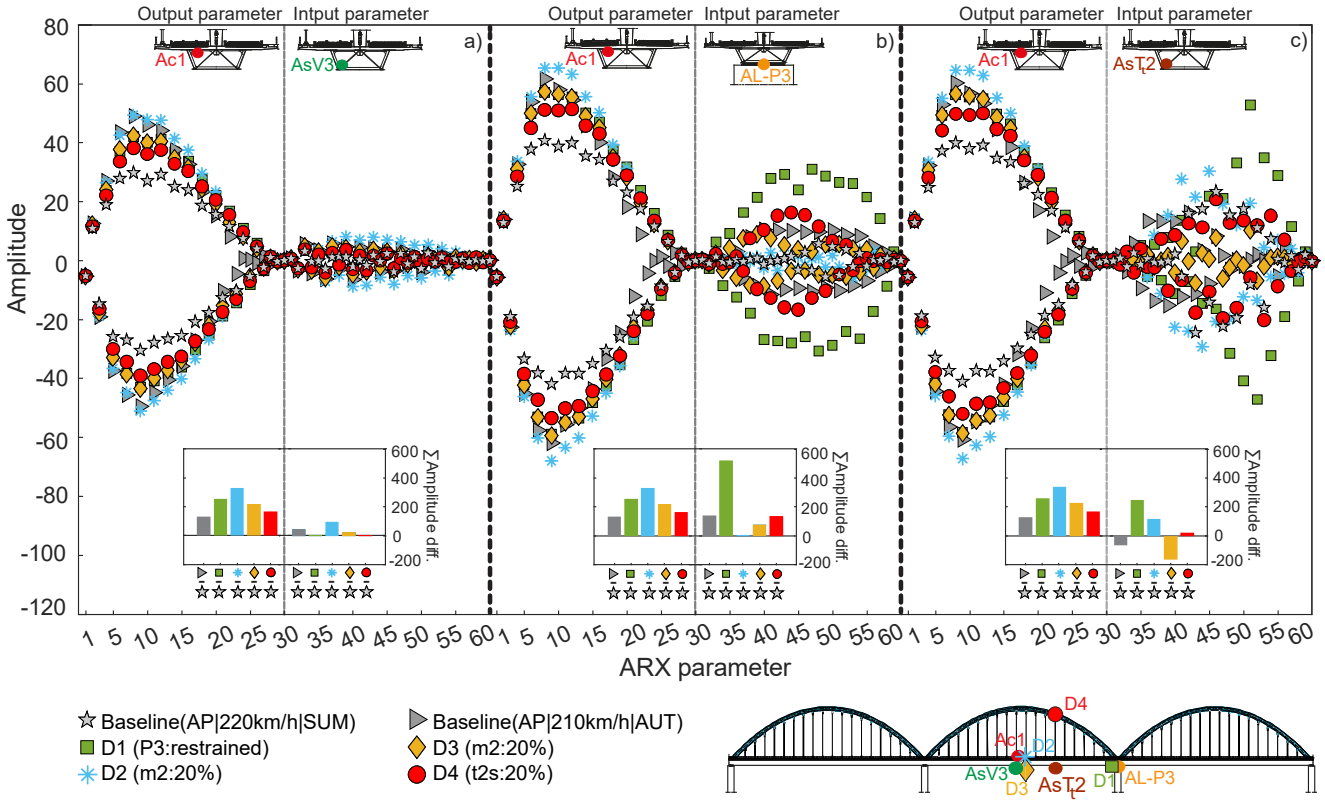

Figure 15. ARX features obtained for the simulated accelerations responses from one output sensor and three different input sensors regarding two baseline and four damaged structural conditions: a) Ac1 and AsV3, b) Ac1 and AL-P3, c) Ac1 and AsT_t2.

The same analysis was conducted for the AR parameters extracted from sensors Ac1 (Figure 16a), AL-P3 (Figure 16b) and AsTt2 (Figure 16c). As with the ARX model, the plots show that the parameters' amplitudes for sensor Ac1, located at mid-span, are those with the most significant changes from one of the baseline scenarios, especially for the damage condition adjacent to this sensor - D2 (m2:20%). A comparison between the bar charts between Figure 16a and Figure 15 indicates a similarity in the relative amplitude obtained when using the signal from sensor Ac1 as output in both the AR and ARX models. Regarding the sensor AL-P3, the features with higher amplitude were observed for the parameters of the damage scenario D1 (P3: restrained), which is the closest to

this sensor. By comparing these results with those obtained with the ARX model (Figure 15b), a considerable decrease in the relative amplitude of the features is observed in the bar chart of Figure 16b. The AR parameters extracted from the transversal accelerometer AsT_t2, located in the steel-box girder at the southern third of the central span (Figure 16c), show more sensitivity to a damage simulated in the same section but in the arch – D4 (t2s:20%) and to a damage in the mid-span of the concrete slab – D2 (m2:20%).

As a result from this study, the clear advantage of crossing information between sensors has shown that ARX models allow for an improvement in terms of the knowledge extracted from the features, which may lead to greater sensitivity.

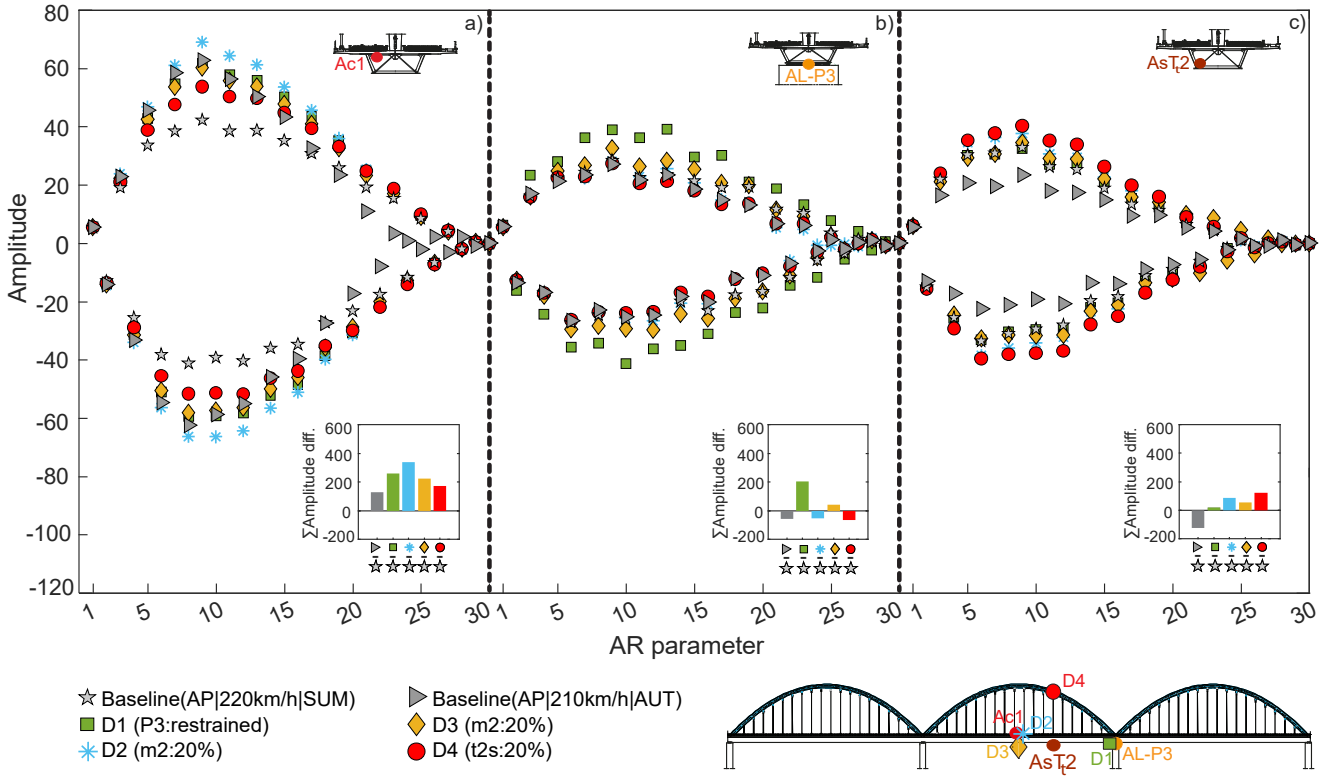

Figure 16. AR features obtained from the accelerations responses simulated at three sensors locations regarding two baseline and four damaged structural conditions: a) Ac1, b) AL-P3 and c) AsT_t2.

3.2 Feature modelling

One of the main obstacles in applying vibration-based SHM systems in operational conditions is the challenge in separating (assumed unmeasured) EOVs from the dynamic responses to obtain features that are primarily sensitive to damage. To overcome this problem, principal component analysis (PCA) [8] is used here for feature modelling. PCA is a multivariate statistical method that produces a set of linearly uncorrelated vectors called principal components (PCs) or scores, from a multivariate set of vector data [34]. PCA can be used to remove the linear effects of EOVs on the responses of the structure during a training period, from which scores are obtained. New effects present in a test dataset, which did not exist in the training dictionary, are highlighted when projected in the subspace of the test dataset [13,35,36]. Considering an *n-by-m* matrix X with the original features extracted from the dynamic responses, where m is the number of ARX or AR parameters and n is the number of simulations for the baseline condition, a transformation to another set of m parameters, Y, designated principal components or scores, can be achieved by the following equation:

$$Y = X \cdot T \tag{4}$$

where T is an *m-by-m* orthonormal linear transformation matrix that applies a rotation to the original coordinate system. The covariance matrix of the ARX/AR parameters in the baseline condition, C, is related to the covariance matrix of the scores, Λ, as follows:

$$C = T \cdot \Lambda \cdot T^T \tag{5}$$

in which T and Λ are matrixes obtained by the singular value decomposition of the covariance matrix C of the ARX/AR parameters. The columns of T are the eigenvectors and the diagonal matrix Λ comprises the eigenvalues of the matrix C in descending order. Hence, the eigenvalues stored in Λ are the variances of the components of Y and express the relative importance of each principal component in the entire data set variation [8].

The PCA is able to retain meaningful information related to EOVs in the first components, whereas variations related to local effects of small-magnitude, such as early-damage, may be summarized in latter components [13]. Since the aim of the present work is to detect damage, the feature modelling procedure consists of removing the most significant PCs from the features. With this in mind, the matrix Λ can be divided into a matrix with the first p eigenvalues and a matrix with the remaining *m-p*. Defining the number of p components remains an open question with regard to the representation of the multivariate data; although several approaches have been proposed, there is still no definitive answer [37]. In the context of SHM, according to Yan et al. [8], the selection of an appropriate dimension p is not so critical as it appear, because what is being looked for is a change in the hyperplane defined by the p principal components adopted from the reference state to the current state. Therefore, stable results can be obtained using different p principal components. In this work, the value of p is determined based on a rule of thumb in which the cumulative percentage of the variance reaches 80% [37,38]. As mention in Jolliffe [38], the justification to implement this rule is mainly because it is intuitively plausible and it works in practice. Choosing a cut-off of 80%, provides a rule which in practice discards in the first PCs most of the information, which is in line with the research detailed in Santos et al [13]. After choosing p, the *m-p* components of the matrix Y can be calculated using Equation (4) and a transformation matrix $\hat{T}$ built with the remaining *m-p* columns of T. Those *m-p* components can be remapped to the original space using the following:

$$F_{PCA} = X \cdot \hat{T} \cdot \hat{T}^T \tag{6}$$

where F_{PCA} is the *n-by-m* matrix of PCA-based features, expected to be less sensitive to EOVs and to be more sensitive to the damage cases. This procedure is repeated for each sensor.

The implementation of the PCA modelling to the ARX parameters resulted in a *22-by-60* matrix with PCA-based features for each train crossing. Since the cumulative percentage of the variance of the sum of the first three principal components was higher than 80% for different structural conditions, these three PCs were discarded during the modelling process (i.e., $p = 3$). The same procedure was applied to the AR parameters and the outcome was a *23-by-30* matrix with PCA-based features. Figure 17a shows four series of parameters, across the 214 scenarios, obtained for an ARX model comprising accelerometer Ac1 (output) and accelerometer AsV3 (input), after the application of the PCA. Figure 17b shows the boxplots obtained from the sixty ARX-PCA-based features. The direct comparison of these action-free ARX parameters (Figure 17) with those shown before applying PCA (Figure 13) shows that, in fact, feature modelling allowed minimizing the differences generated by the effects of train type and speed and by temperature, shown in grey box-and-whiskers plots, which significantly reduce from one figure to the other. The same is not observed in the features from damage cases, represented in

green box-and-whiskers plots, which remain identical or even increase. As corroborated by Figure 17b, the EOVs were mitigated and a clear improvement is obtained, especially for the first thirty parameters (the output), which after feature modelling reveal distributions that are similar to those from the thirty input parameters (ARX31-ARX60).

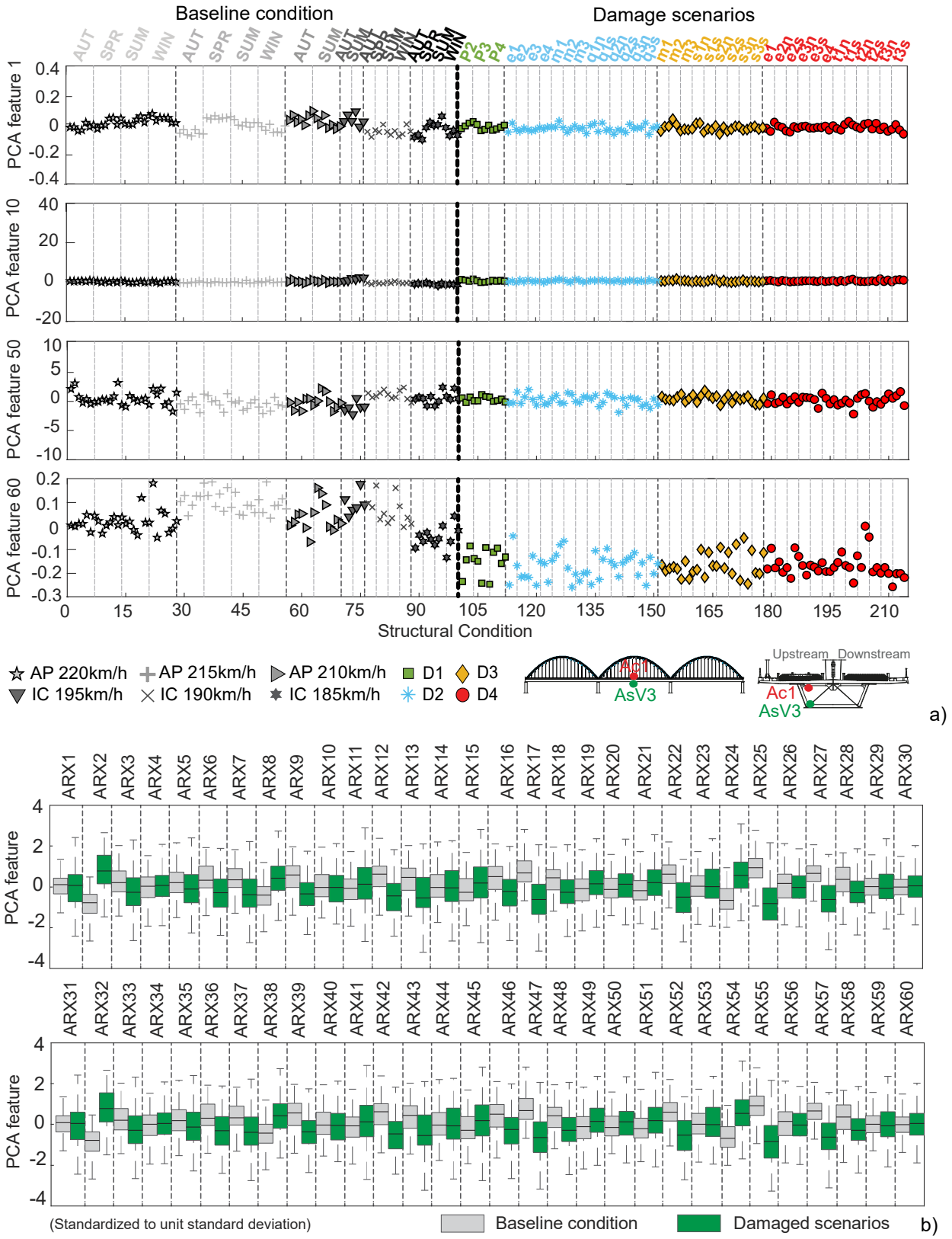

Figure 17. For all 214 structural conditions considering the simulated responses of accelerometer Ac1: a) amplitude of four of the sixty ARX-PCA-based features, b) box-and-whiskers plots representing the sixty ARX-PCA-based features.

Figure 18 shows two AR parameters for accelerometer Ac1, obtained after applying the PCA-based modelling, and the thirty box-and-whiskers plots for the thirty AR-PCA-based features. The comparison of these plots with those shown in Figure 14 shows the suppression of the changes generated by EOVs; however, an improvement between the distributions of the baseline simulations and the damage scenarios is not as clear as that obtained with the ARX-PCA-based modelling (Figure 17b).

Nevertheless, the differences between the several structural conditions, after PCA implementation, are not enough to allow for a clear distinction between undamaged and damaged scenarios, either for ARX or AR parameters. In this sense, a data fusion is performed and discussed in the next section.

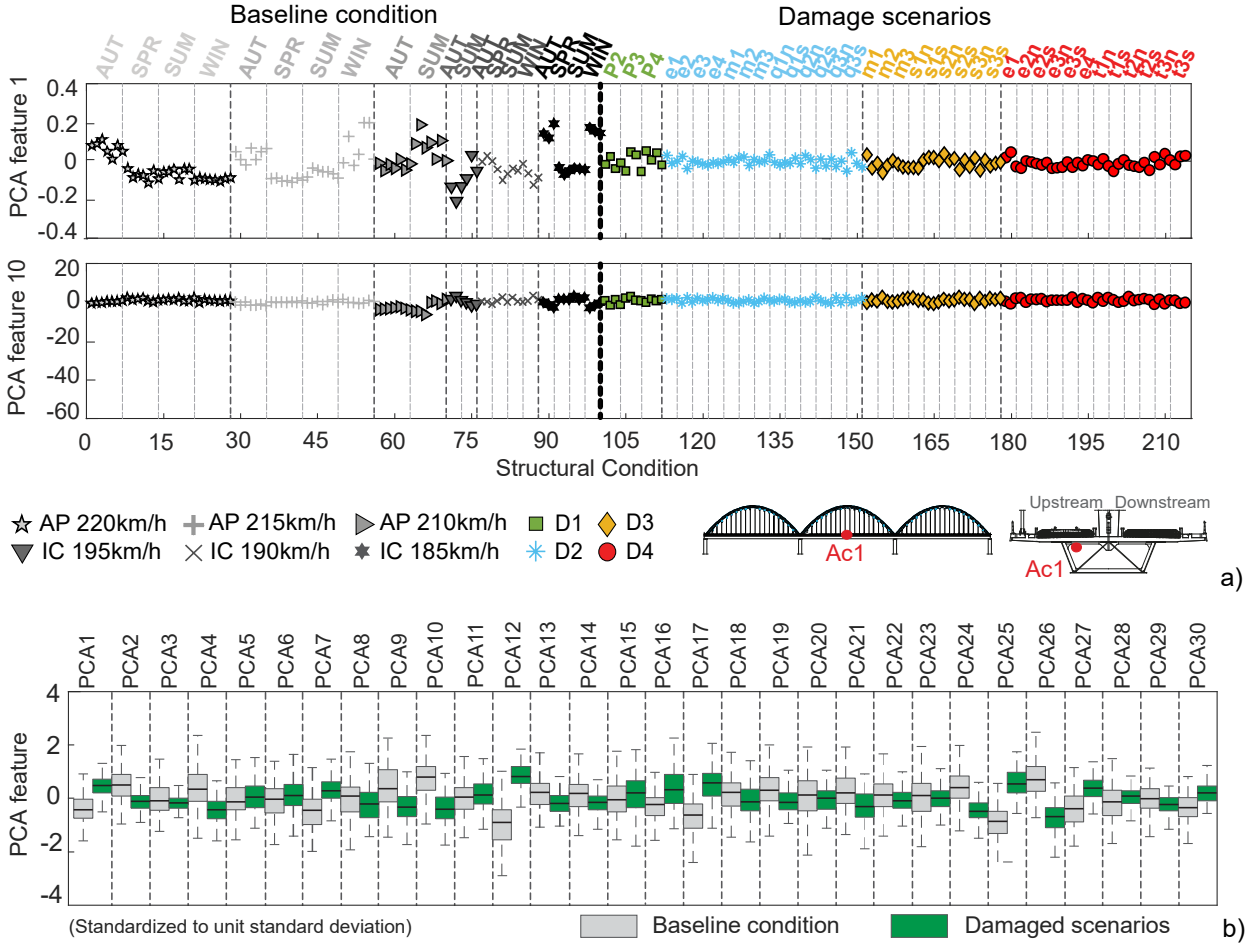

Figure 18. For all 214 structural conditions considering the simulated responses of accelerometer Ac1: a) amplitude of two of the thirty AR-PCA-based features, b) box-and-whiskers plots representing the thirty AR-PCA-based features.

3.3 Data Fusion

To fuse the data obtained from all AR/ARX parameters and describe the variability present in the features, a Mahalanobis distance (MD) measure was computed on the PCA estimation errors. The MD consists of a weighted metric, used herein as damage indicator, in which the weights are determined by the covariance structure. The weighting proportional to the covariance structure provides an additional layer of feature modelling which, when defined for regular actions, allows outlining with high sensitivity those that were not used for the definition of the covariance structure. Thus, the MD was selected since it is based on the AR/ARX parameters' centre and covariance, therefore enabling additional sensitivity if these quantities are computed using only the AR/ARX parameters extracted from the baseline conditions. With this approach, the MD measures the distance between the representative baseline and each set of features extracted from a train crossing. Smaller MD values represent

greater similarities with the representative baseline, while higher values reveal greater differences, and, therefore, more dissimilar structural conditions. The analytical expression of MD for each simulation i is given by

$$MD_i = \sqrt{(x_i - \bar{x}) \cdot {S_x}^{-1} \cdot (x_i - \bar{x})^T}, \quad (7)$$

where x_i is a vector of m features representing the potential damage/outlier, $\bar{x}$ is the matrix of the means of the features estimated on baseline simulations, and S_x is the covariance matrix of the baseline simulations.

The MD allows transforming, for each sensor and for each train crossing, the 60 ARX-PCA-based parameters into one single distance-based feature; this feature exhibits higher values for distinct structural conditions and nominal values for identical structural scenarios. The outcome of this procedure is a 214-by-1 vector of distances for each sensor. The three plots in Figure 19a clearly show a sensitivity improvement for sensors' cluster Ac1+AsV3, Ac1+AL-P3, and Ac1+AsT$_t$2 to each structural condition. A variation among the values of the Mahalanobis distance for the damage scenarios can be observed for the three sensors' clusters. Two main aspects can explain this behaviour: (i) the diversity of damages simulated, which are different in nature, type and location across the structure, as detailed in section 2.2, and (ii) the sensitivity of the ARX-based features.

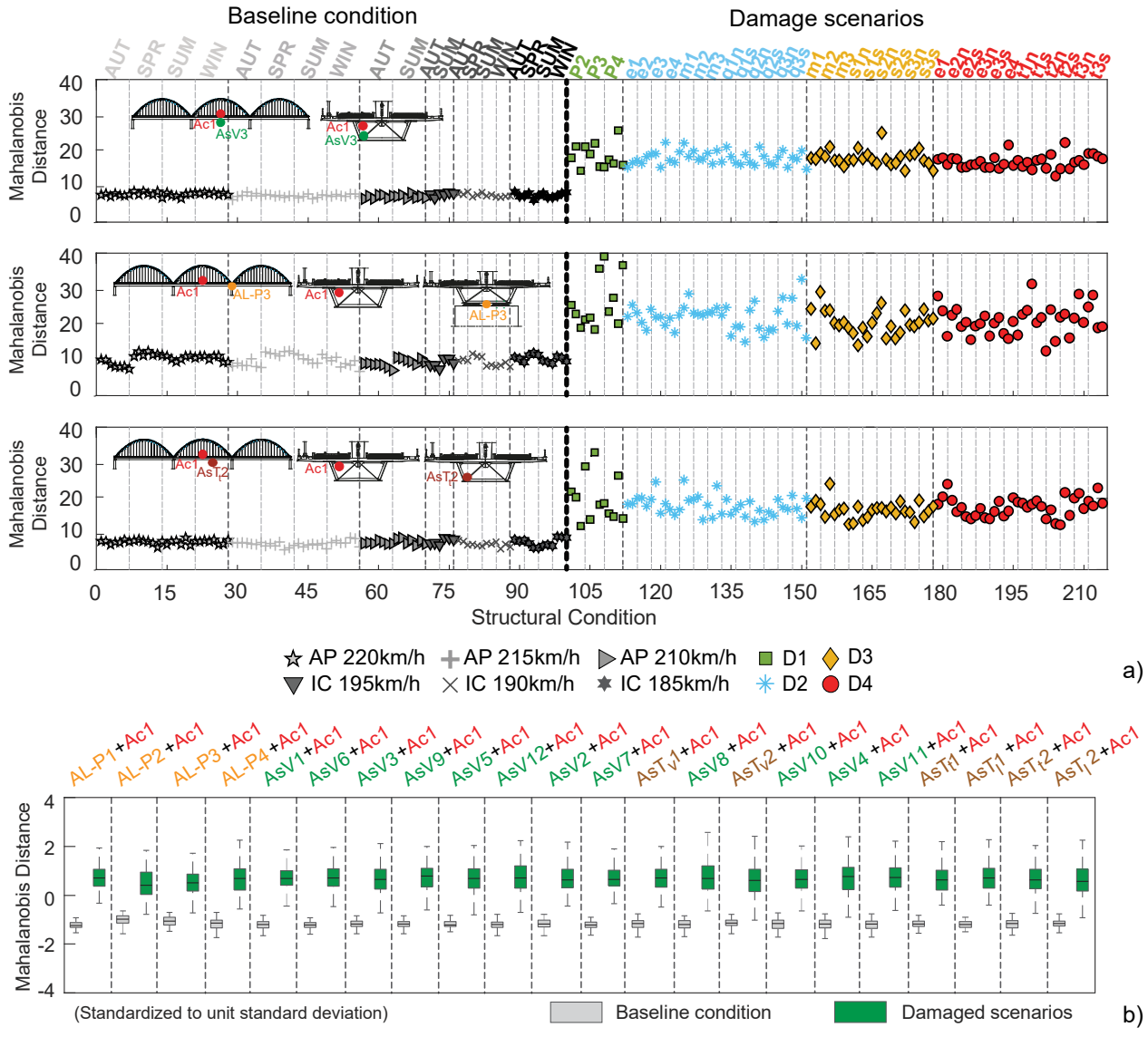

Figure 19. Mahalanobis distance of the ARX-PCA-based features for all 214 structural conditions: a) considering the simulated responses from accelerometers Ac1+AsV3, Ac1+AL-P3 and Ac1+AsTt2, b) box-and-whiskers plots for each sensor combination.

In addition, Figure 19a corroborates that different sensors show different sensitivity to the damage, which leads to different variations in the Mahalanobis distance. Figure 19b shows the distribution obtained from each of the twenty-two sensors' clusters (with the locations presented in Figure 2), which suggests an evident separation between the simulations of the baseline condition and the damage scenarios.

The same procedure was applied to the 30 AR-PCA-based features, which also resulted in a 214-by-1 vector of distances for each sensor. Figure 20a shows a sensitivity increment of each sensor in distinguish baseline from damaged conditions, especially when observing the distributions in Figure 20b. However, there is an undeniable superior performance of the ARX model when comparing both outcomes. For this reason, the online SHM procedure described hereafter was based on damage-sensitive features extracted from the ARX model.

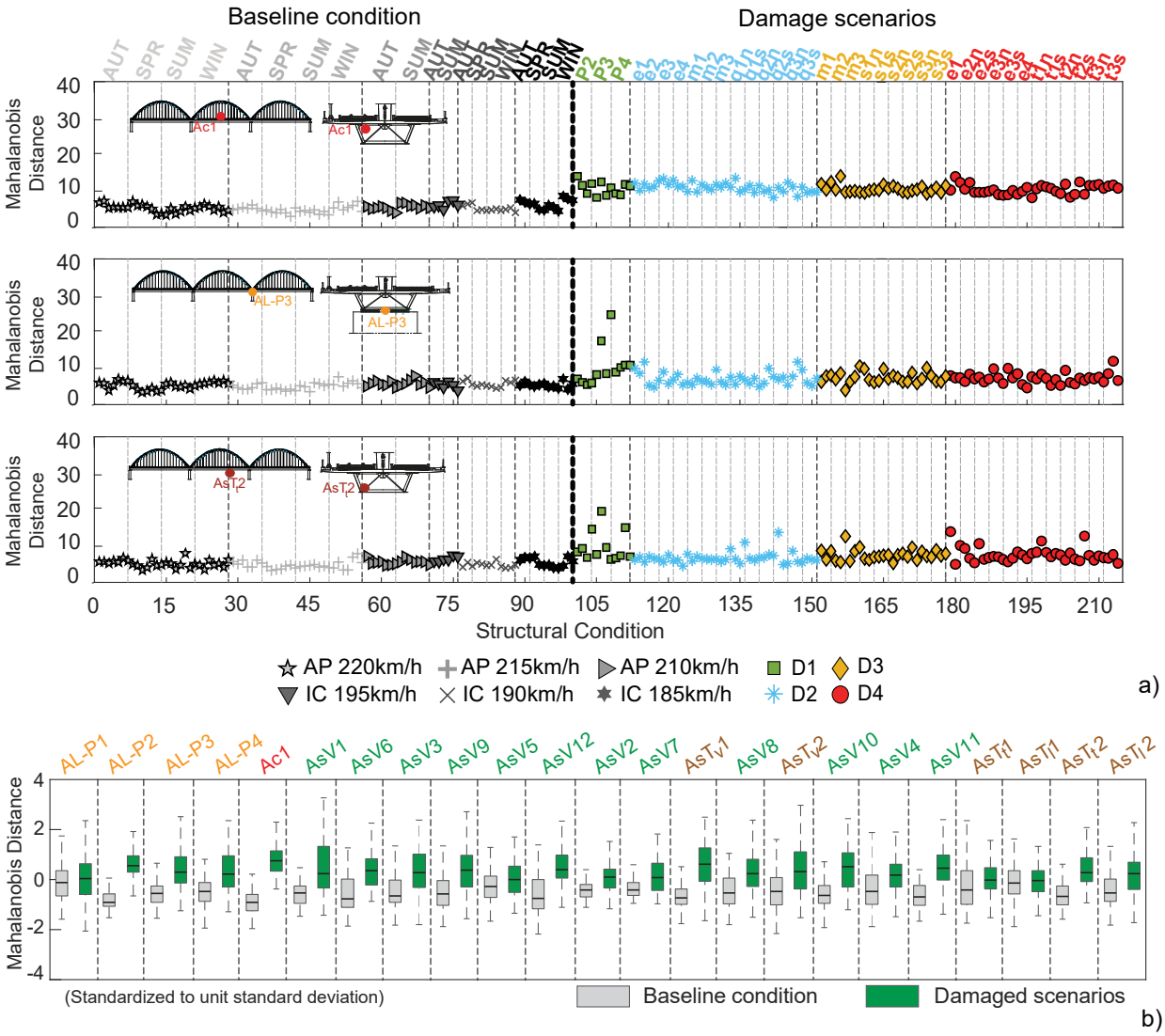

Figure 20. Mahalanobis distance of the AR-PCA-based features for all 214 structural conditions: a) considering the simulated responses from accelerometers Ac1, AL-P3 and AsTt2, b) box-and-whiskers plots for each sensor combination.

3.4 Feature discrimination – cluster analysis

Times-series analysis and distance measures can help perform data analysis and suggest the existence of different structural behaviours within a data set, as shown in the previous sections. However, the development of online SHM strategies should resort to machine learning algorithms that can autonomously decide whether one or more distinct structural behaviours are being observed from patterns in the features. Hence, feature discrimination is addressed herein using unsupervised discrimination algorithms - cluster analysis.

The aim of the clustering process is to divide a dataset into groups, which must be as compact and separate as possible [39]. This can be mathematically posed as an attempt to minimize the dissimilarity between features assigned to the same cluster (within-cluster distance), which, consequently, maximizes the dissimilarity between the features assigned to different clusters (between-cluster distance) [40]. Considering a given partition containing K clusters, $P_k = \{C_1, \dots, C_k\}$, the overall within-cluster dissimilarity $W(P_k)$ and the overall dissimilarity OD can be defined as:

$$W(P_k) = \frac{1}{2}\sum_{k=1}^{K}\sum_{c(i)=k}\sum_{c(j)=k} d_{ij} \tag{8}$$

$$OD = \frac{1}{2}\sum_{i=1}^{N}\sum_{j=1}^{N} d_{ij} \tag{9}$$

in which the between-cluster dissimilarity is given by the subtraction $B(P_k) = OD - W(P_k)$. Here, N is the total number of features and $c(i)$ is a many-to-one allocation rule that assigns feature i to cluster k, based on a dissimilarity measure d_{ij} defined between each pair of features i and j [41]. The best-known clustering algorithm is iterative and called k-means [42]. The k-means requires that the number of $K < N$ clusters be initially defined along with a randomly defined set of K clusters' prototypes. This task is called initialization. Afterwards, each iteration starts by allocating the features to the clusters according to an allocation rule, $c(i)$, that assigns each feature to the least dissimilar (closest) cluster prototype. The second step of each k-means' iteration is called representation and consists of defining the centroids of the K clusters as their prototypes and assuming that each feature belongs to the cluster whose prototype is closest. These two steps, allocation and representation, are subsequently repeated until an objective function, which depends on the compactness and separation of the cluster, reaches its global minimum value. The k-means considers the squared within-cluster dissimilarity measured across the K clusters as an objective function [42]. Clusters' dissimilarities are generally defined as distance metrics. Among these, the Euclidean (square root of the sum-of-squares) is used here.

Using the features shown in Figure 19 for all sensor clusters, the dissimilarities between undamaged and damaged conditions can be computed and represented in distance matrices. Figure 21a presents the matrix for baseline conditions, while Figure 21b shows the matrix considering baseline and damaged structural conditions, where dark blue represents the null distance (identical features) and yellow represents the most dissimilar features of the analysed sample set (maximum distance). A straightforward observation of Figure 21b allows conclusions to be drawn regarding the existence of two compact groups of samples: darker regions within the matrix separated by lighter regions of the same matrix. These two groups correspond unmistakably to the two distinct structural conditions simulated: damaged and undamaged (baseline). It can also be observed that the baseline group of features is much more compact than the set of damage-related features, since the first consists of a darker blue colour, while the second exhibits greener areas since it is composed of numerous distinct structural conditions. Conversely, Figure 21a reveals a uniform distribution of colours throughout the entire sample set, suggesting that no changes occurred in the structure during those train crossings.

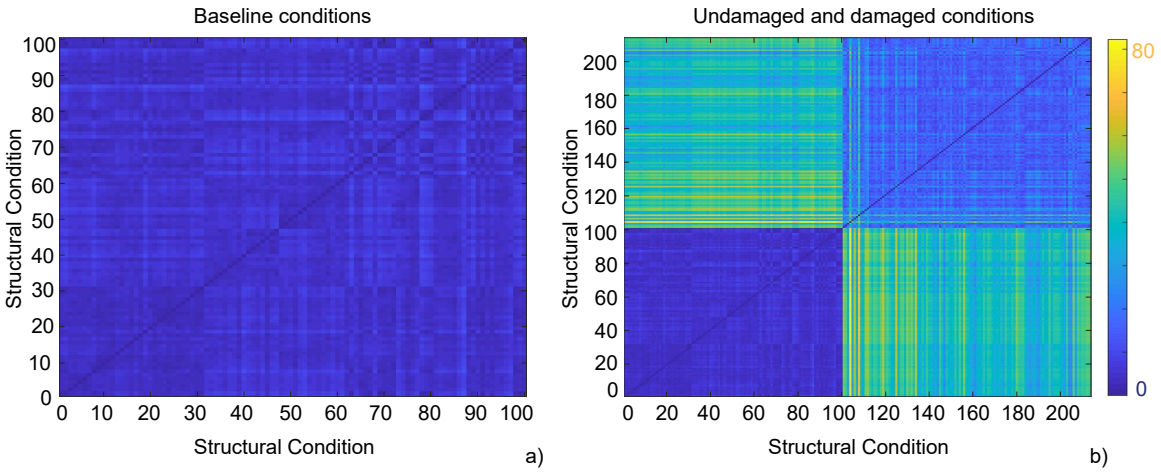

Figure 21. Dissimilarity matrices obtained from: a) baseline conditions, b) undamaged and damaged conditions (dark blue=identical features, yellow=most dissimilar ones).

As previously mentioned, the k-means clustering method requires that the number of clusters be defined in advance and provided as input (in the initialization phase). For damage detection, there is no way of knowing this number in advance [43], which requires that multiple partitions, comprising different numbers of clusters, be tested and their outcomes analysed using cluster validity indices [42]. Numerous validity indices have been proposed and tested, not only in specific literature but also in SHM applications. Herein, the global silhouette index (SIL) is used, since it revealed a superior performance in previous studies [12,43], in which its formulation is carefully described. The application of the k-means along with the SIL index is exemplified here using the features (Figure 19) extracted from the sample time-series. For the present paper, it is important to note that, among the K tested, the partition that generates the highest SIL value is the one that best describes the analysed features set [39], and should, therefore, be considered for SHM purposes. Using the features shown in Figure 19, the SIL indices extracted from five cluster partitions, shown with 'o' marks in Figure 22a, exhibit a maximum for $k = 2$ clusters. The corresponding features' allocations were automatically generated by the k-means method and are shown in Figure 22b and Figure 22c. These plots demonstrate that the clustering method is capable of dividing the features without any human interaction or input. Figure 22b shows the dissimilarity between the two centroids, while in Figure 22c it can be observed that the two clusters found are compact over time and separated when the simulated damages start. This result undeniably shows that the k-means method is capable of analysing the features set and, in a fully automated manner, separating it according to the structural conditions observed on site.

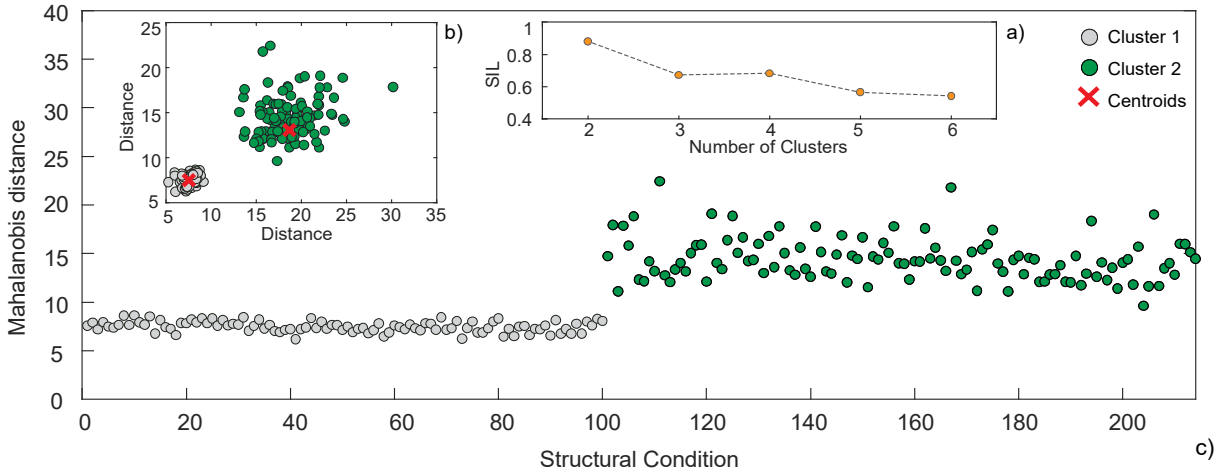

Figure 22. Allocation of damage-sensitive features into clusters: a) silhouette index (SIL), b) clusters centroids, c) clusters defined for all structural conditions.

4. Online procedure for damage-detection

4.1 Proposed methodology

In the previous section, it was demonstrated that the combination of the ARX model, PCA, and data fusion is effective in extract and modelling features and detecting damage under a variety of confounding EOV conditions. It was also observed that the cluster analysis is capable of automatically distinguishing between baseline and damaged conditions. However, the output of cluster analysis requires user intervention to assess whether clusters are compact or dispersed over time, and therefore difficult to apply in automated online SHM. To circumvent this limitation, instead of relying on the allocation of features to clusters over time, the average dissimilarity between clusters, DC, is computed [12]:

$$DC = \frac{1}{K(K-1)} \sum_{k=1}^{K} \sum_{\substack{c=1 \\ c \neq k}}^{K} d_{ck} \tag{10}$$

where K is the number of clusters belonging to the partition with the highest SIL, c and k are two of the K clusters, and d_{ck} is the dissimilarity measured between their centroids. If no damage occurs and the structural behaviour remains unchanged (as in Figure 21a), the clusters generated by the k-means are similar and will generate small DC values. Conversely, if damage is observed, the k-means generates dissimilar and separate clusters (as in Figure 21b) and, consequently, large DC values.

The procedure proposed aims to provide continuous binary information of the type TRUE/FALSE regarding the existence of damage. It consists in successively extracting parameters from time series, statistically modelling the features, and classifying the structural response, using the algorithms described in section 3, within moving windows of SHM data to obtain a set of DC values. These windows are defined with a fixed number of train crossings. Due to the fact that the DC value does not provide TRUE/FALSE information on its own, the proposed methodology requires an additional step. It consists of statistically testing the DC values obtained within each window's length. The statistical testing of each set of DC values results in the definition of a confidence boundary (CB), which is exceeded only if the target structural system exhibits changes. The CBs are defined by statistically testing the DC distribution, under the premise that residual errors obtained from unchanged structures are only influenced by random effects. This premise is commonly used in SHM works addressing damage detection [36,37]. Generally, the literature refers that the Mahalanobis squared distance can be approximated by a chi-squared distribution in n-dimensional space. Thus, since the chi-squared distribution models the sum of squares of independent random variables (gaussians), it can be considered that the Mahalanobis distance can also be approximated by a Gaussian statistical distribution [12,43,46,47]. Under this hypothesis, a confidence boundary (CB) to detect a DC that constitutes an outlier can be estimated by the Gaussian inverse cumulative distribution function considering a mean μ and standard deviation σ of the baseline DC vector, and for a level of significance α. The selection of α carries a trade-off between the Type I error (*false-positive* indication of damage) and the Type II error (*false-negative* indication of damage) [2]. The inverse function can be defined in terms of the Gaussian cumulative distribution function as follows:

$$CB = invF(1-\alpha) \tag{11}$$

where

$$F(x|\mu,\sigma) = \frac{1}{\sigma\sqrt{2\pi}} \int_{-\infty}^{x} e^{-\frac{1}{2}\left(\frac{x-\mu}{\sigma}\right)^2} dy, for\ x \epsilon \mathbb{R} \quad (12)$$

The moving windows procedure proposed is detailed in the flowchart of Figure 23 and is divided into two main stages: a) the baseline and CB build and b) the online damage detection.

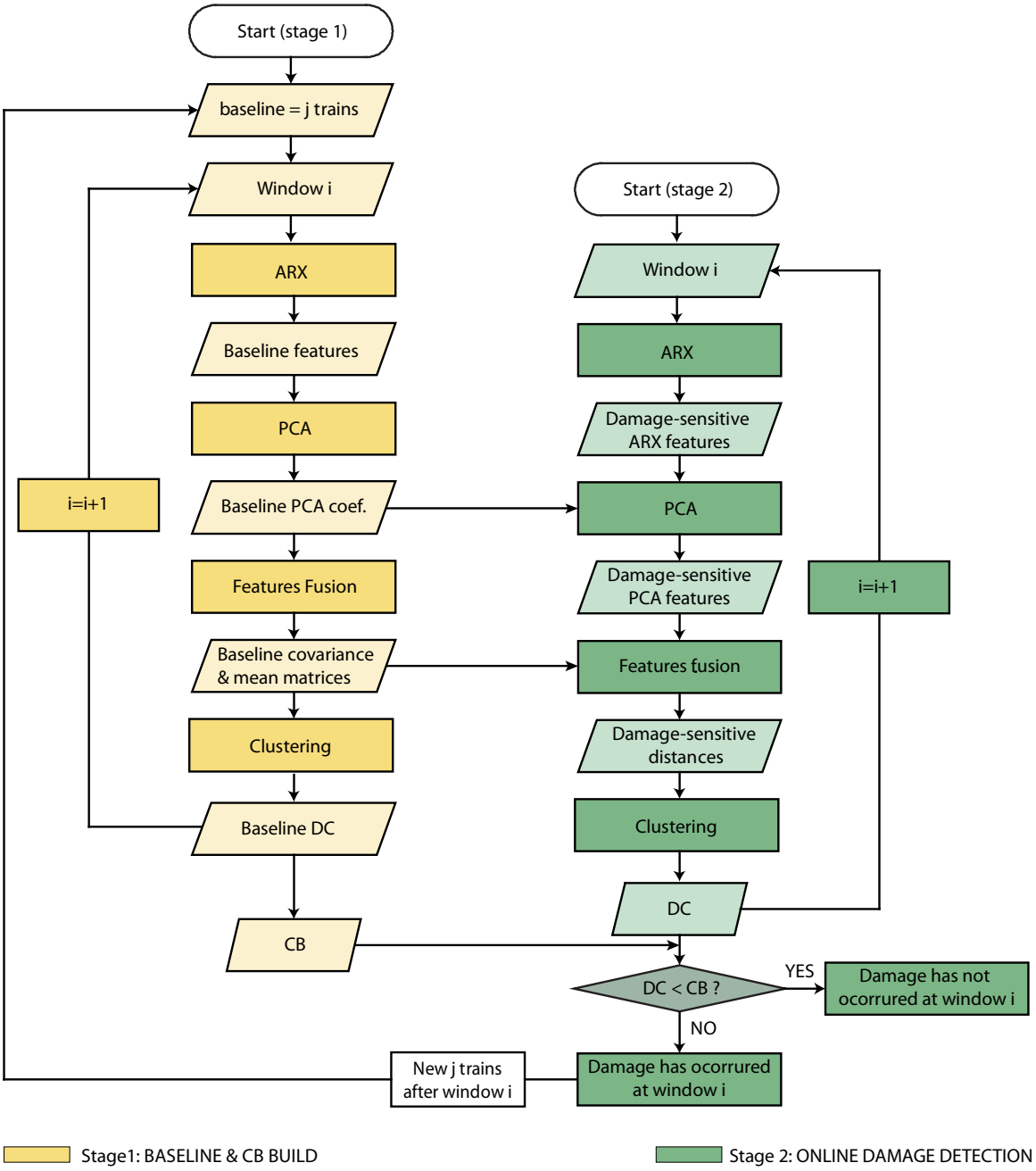

Figure 23. Flowchart of online damage detection procedure based on moving windows.

After the initialization, which consists of defining the total number of trains crossings, j, that compose the baseline, as well as the number of trains crossings within each window, the machine learning strategy described in section 3 is applied to the responses measured during the passage of the trains within each window i. During the first stage, the coefficients of PCA and the covariance and mean matrices of the baseline features are computed. At the end of this stage, the baseline DC vector is achieved and used to estimate the CB. During the second stage, the moving windows process is implemented in real time, and the machine learning strategy previously detailed is implemented in each window i. Here, after extracting the ARX parameters from the window's time series, the baseline PCA transformation is obtained, and the baseline covariance and mean

matrices are used for MD-based feature fusion. The corresponding damage-sensitive distances are used as inputs for clustering. The outcome of the windowing process consists of one DC value per window i, and the detection is based on comparing each of these values with the CB. An average distance between clusters DC lower than CB suggests that the changes measured during the corresponding window i were generated by EOVs and, consequently that the structure may be assumed to be unchanged during that window. Conversely, a DC higher than the CB suggests the occurrence of damage during the same period. In the case of damage detection, after j train crossings a new baseline may be defined, which will allow to identify when a new type of damage occur.

The DC series obtained for unchanged structural conditions and for four type of damages, D1 located in pier P4, D2 located in the first mid-span of the concrete slab (m1), D3 located in the diaphragm at 1/6 north of the third span (s3n) and D4 located in the arch at 1/3 south of the second span (t2s), are shown in Figure 24 as examples. These were achieved considering the responses of all sensors installed on site, $j = 100$ trains for the baseline, moving windows with 15 trains and the CB was defined with a significance level of 5%. Figure 24 proves the efficiency of the online procedure to detect different types of damage with different severities, since for each type of damage, each symbol represents a different severity, increasing from left to right (μ=1.8%, μ=2.4%, μ=3.0%, μ=full restrain for D1; 5%, 10% and 20% for D2, D3 and D4). It is interesting to observe that, with the exception of damage D2, the value of DC increases with the severity. Bearing in mind the small severity of the damages simulated and the realistic character of the numerical simulations conducted (Section 2.2), which include the effects of noise, temperature, and train loading measured on site, it can be concluded that the proposed methodology is highly sensitive to damage because it allows detecting stiffness reductions as small as 5%.

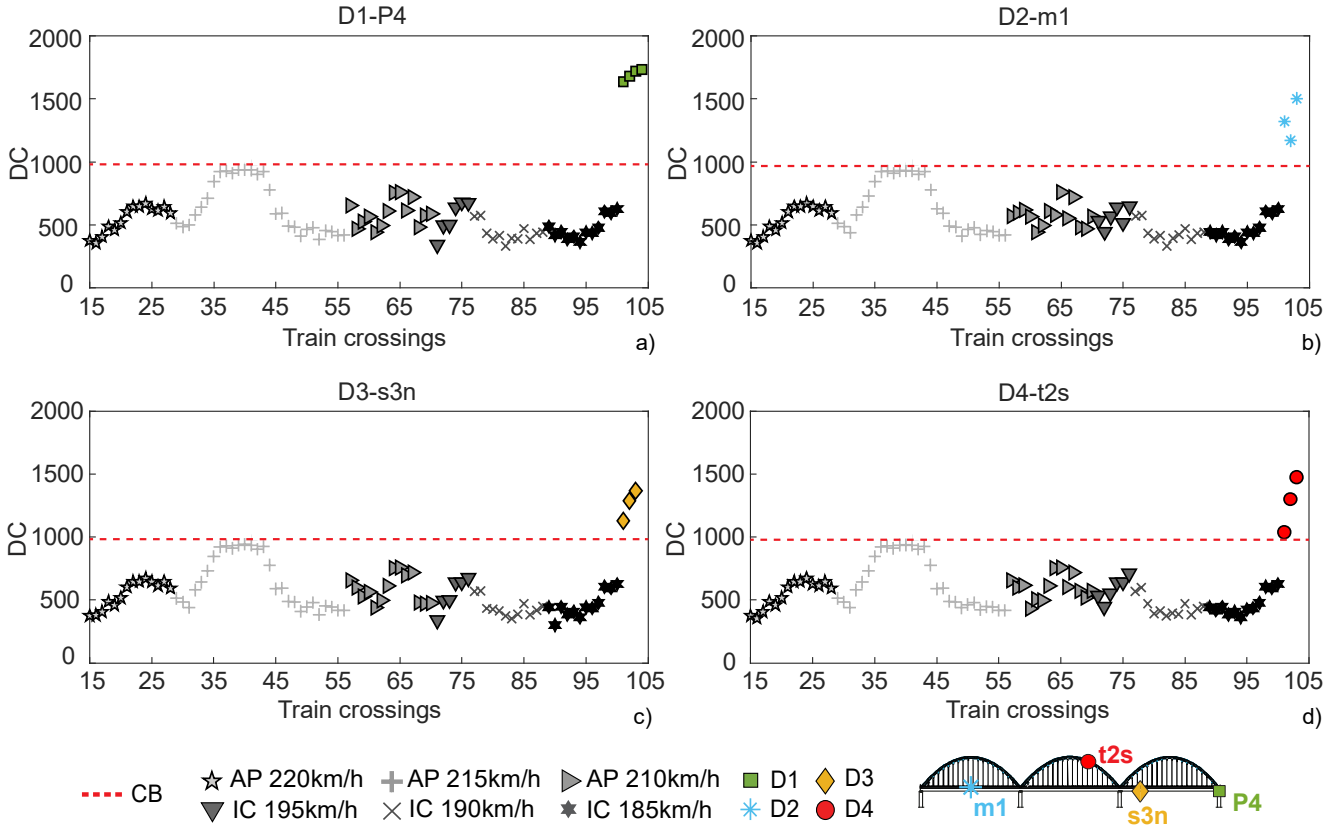

Figure 24. DC values obtained considering four types of damages with different severities: a) D1-P4: μ=1.8%, μ=2.4%, μ=3.0%, μ=full restrain, b) D2-m1: 5%, 10%, 20%, c) D3-s3n: 5%, 10%, 20% and d) D4-t2s: 5%, 10%, 20%.

4.2 Sensitivity to different damage locations

To evaluate whether the results achieved so far may be generalized to different damage states, a more extensive sample of structural conditions (described in section 2.2) was tested and applied to the same damage detection methodology. The 114 online analyses conducted herein comprised 10146 windows, each with 15 trains. Several unchanged structural conditions were already evaluated in Figure 24, and no false positive was obtained; only the sensitivity to new damage scenarios was evaluated using the same window size and the DC values extracted immediately after a damage incidence. These DC values are presented in Figure 25, as well as the corresponding CB, and show that, even if the single-valued DC represents the responses acquired from multiple sensors, it is sufficiently sensitive to highlight small magnitude damage with local character and in different structural elements. Only five false negatives were verified in a total span of 114 very different damage scenarios, namely, two in the concrete slab, one in the diaphragm and two in the arches, all with a stiffness reduction of only 5%. These results strongly suggest that the proposed methodology is, in fact, robust and may be used for damage detection throughout the entire structural system.

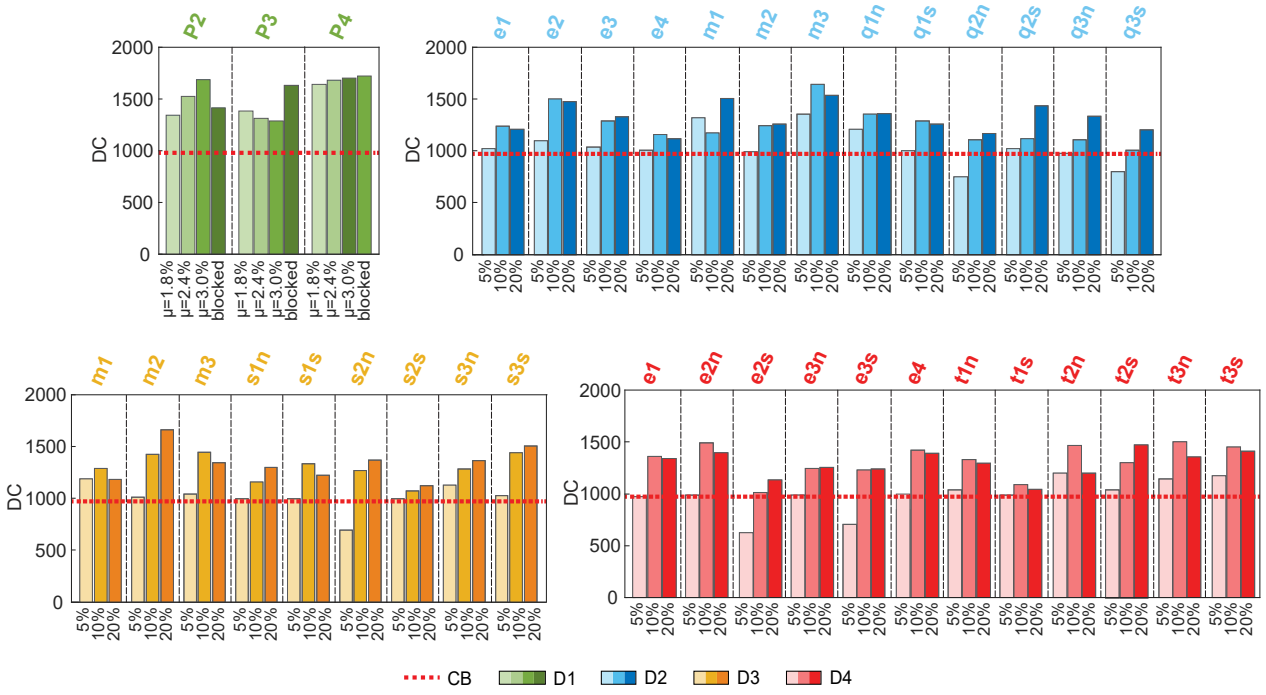

Figure 25. DC values obtained considering four types of damage (D1, D2, D3 and D4) with different severities (D1: μ=1.8%, μ=2.4%, μ=3.0%, μ=full restrain, D2 to D4: 5%, 10%, 20%) in all the locations shown in Figure 6b.

4.3 Assessing the most robust window lengths

The example presented in section 4.2 showed that the proposed methodology was capable of detecting a 5% to 20% stiffness reduction, as well as different bearing restraints, in four types of damage (D1, D2, D3, D4) and in different locations, with a low number of false detections. This performance is, however, affected by the number of trains per window. The trade-off between detection rapidity and robustness is next studied by applying the damage detection procedure using windows with different lengths, i.e., with a varying number of trains per window between six and twenty. As in Figure 25, the simulated responses of all accelerometers deployed on site were considered and a total of 1710 DC vectors (114 different damages and 15 different windows lengths) were obtained from 155610 independent windows. The results achieved with this analysis are summarized in Figure 26, where the percentage of false detections, taken as the incidence of false positives (false damage alerts) and

false negative occurrences (true damage states that were not detected by the method), depending on the length of the window, is presented. The bars in this chart show that important amounts of false detections are obtained for window lengths between 6 and 13 trains, both for undamaged and damaged scenarios. Also, it is shown that most of the false detections are related to damage in the concrete slab (D2) and in the arch (D4). This can be associated with the sensor locations, since no sensor has been installed in the arches, and the concrete slab has only one sensor located in the second mid-span. With a window length of 14 trains, false detection reduces to 6%, but it is with a window of 15 trains that only 2% of false detections are reached, which corresponds to a most robust detection process. As presented in Figure 25, these 2% are associated with damages with a severity of only 5%. The analysis was also performed for windows including 16 to 20 trains, but the improvement in terms of false detections was residual, if not null, which suggests that a substantial number of additional trains would be needed to achieve a 0% of false detections.

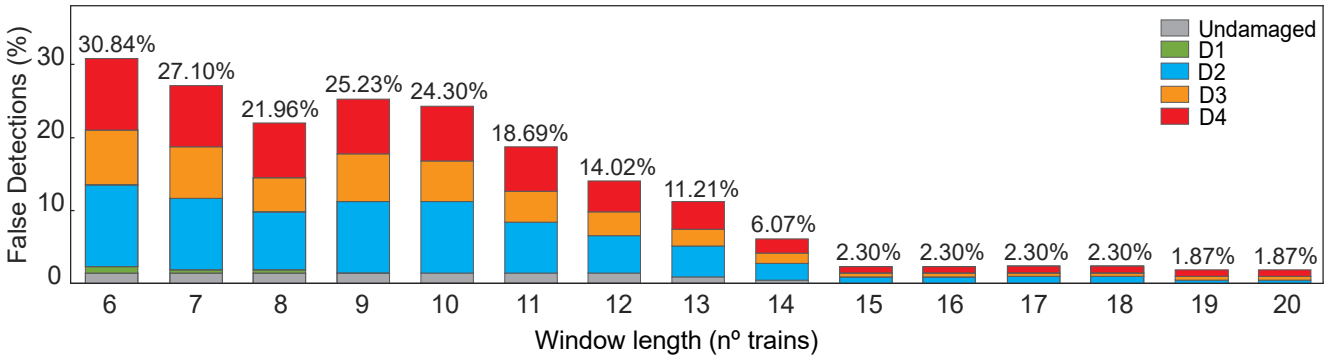

Figure 26. Percentage of false detection incidences depending on the window length.

4.4 Studying the effectiveness of smaller sensor networks

To assess whether the number of sensors used to detect different types of damage may be optimized, a study of the false detection incidences as a function of the monitoring system configuration is considered. The main goal is to analyse the trade-off between the optimization of the sensing system (which leads to a cost reduction in terms of the monitoring system installation) and the effectiveness of the damage detection procedure. For all structural conditions mentioned in the previous sections, the online damage detection procedure was applied with a window length of 15 trains, but considering the responses obtained with four possible configurations of an SHM system progressively adjusted for smaller numbers of sensors than those installed on site. Figure 27 shows the percentage of false detections got for each configuration, with the lowest value (2%) achieved with the 23 accelerometers currently installed on site. If the vertical accelerometers installed on the downstream side of the steel box-girder were removed, there would be a 2% increase in false detections. The third SHM system configuration also excludes the vertical accelerometers located at 1/3 of the first and third spans and leads to an increase of 1% in the false detections. Finally, if only seven sensors remained, namely, the longitudinal accelerometers on the four piers, the vertical accelerometer on the second mid-span of the concrete slab, and the vertical accelerometers in the steel box girder at each mid-span, 7% false detections would be observed. It is worth noticing that among the four configurations, the increment of false detections with the reduction of the number of sensors only happens for damage cases with a 5% severity. Moreover, in the event of sensor malfunction or maintenance, even with a reduction of the number of sensors in 30% there is only an increase of 5% in false detections.

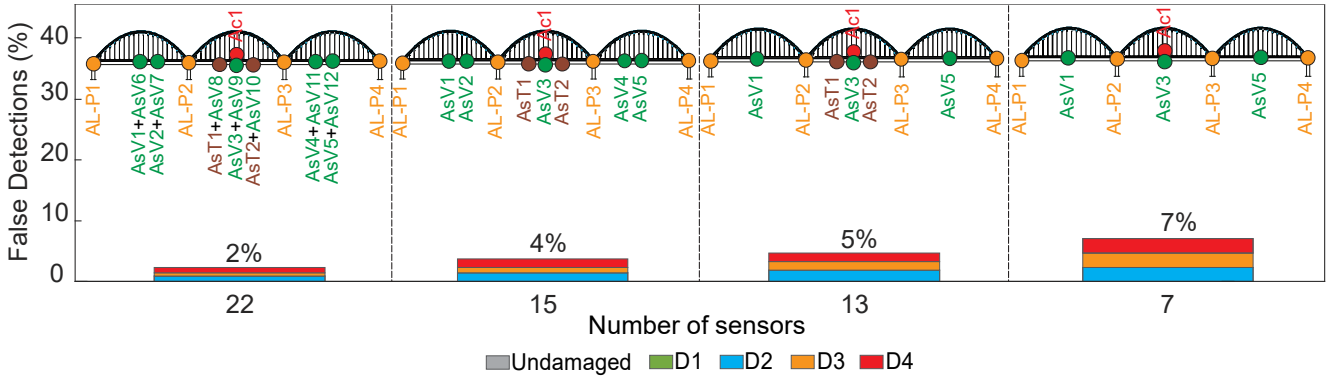

Figure 27. Percentage of false detection incidences depending on the number of sensors.

4.5 Defining an adaptive confidence boundary

Thus far, the proposed online damage detection strategy was applied considering a single CB build based on responses from unchanged structural conditions. However, in case a specific type of damage occurs, it is desirable for the CB to adapt in order to detect future damage that may arise over time. Figure 28 shows an application of CB progression, where additional damage scenarios (types D1, D2, D3 and D4) were simulated to apply this procedure.

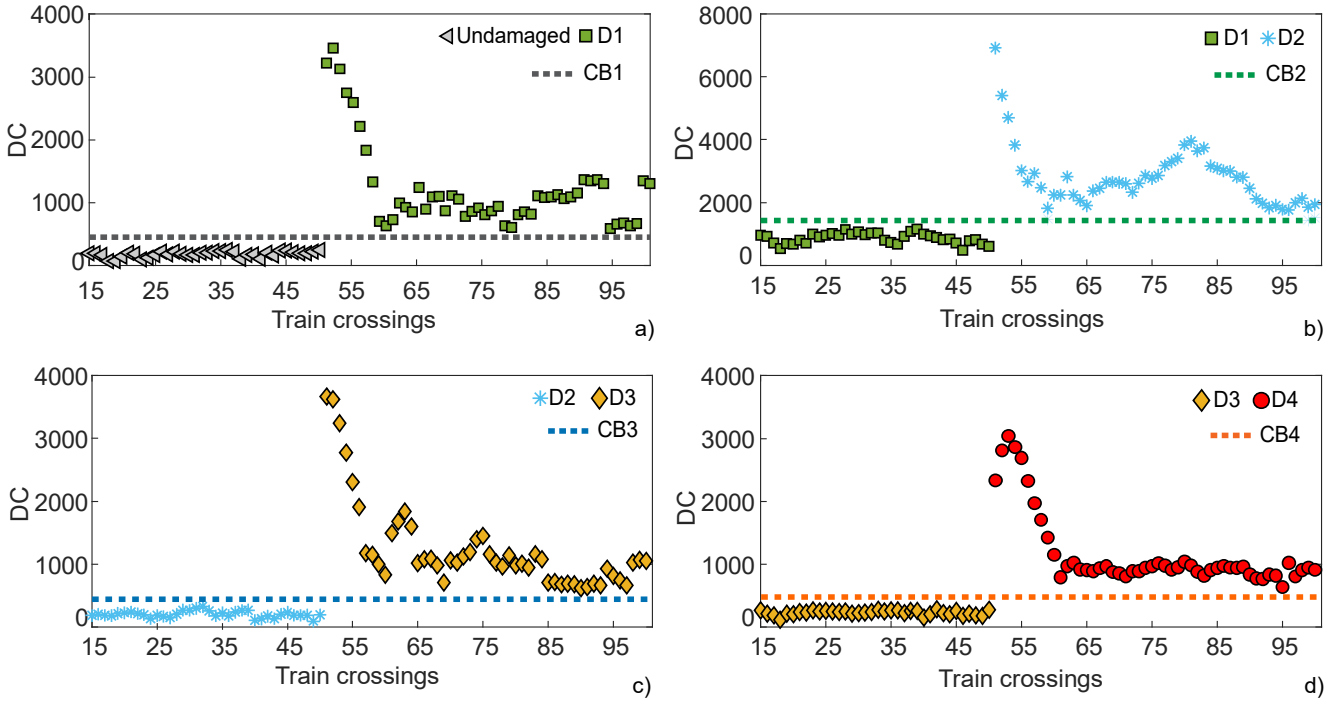

Figure 28. Adaptive CB for different types of damage: a) undamaged vs D1, b) D1 vs D2, c) D2 vs D3 and d) D3 vs D4.

In Figure 28a, the CB1 was defined, as in the previous sections, for the baseline (undamaged) condition using 50 trains crossings and a time window of 15 trains. The application of the damage detection online procedure proposed lead to the substantially increase of the DC values and exceedance of the CB1, when a train crosses the bridge with a damage in the bearing of pier P4 (D1). The DC values progressively decrease as the windows contain more trains from a damaged structure than for a baseline condition. In Figure 28b, a new baseline and confidence boundary (CB2) were defined using the bridge response from the 50 train crossings while the damage in the bearing of pier P4 (D1) was active. This new baseline containing PCA coefficients and Mahalanobis distances with the new covariance and mean matrices from the bridge responses with the damage D1 allowed defining a new confidence boundary (CB2) and detecting the new type of damage that occurred in the concrete slab (D2). Afterwards, the CB3 was built considering the new 50 trains crossings with the structure damaged on

the concrete slab (D2), and a damage on the diaphragm (D3) was later detected (Figure 28c). The same strategy was applied to detect a damage on the arch (D4) after a damage on the diaphragm (D3) has occurred (Figure 28d). This analysis proves the efficiency of the adaptive CB in automatically detecting new types of damage.

5. Discussion

Civil structures tend to be one-of-a-kind, large capital assets, that are generally kept in good condition by the managers with appropriate inspection and maintenance actions. Consequently, bridge data acquired under damaged conditions is generally scarce. Therefore, the effectiveness of the strategies similar to the one proposed herein tend to be validated using digital twins, such as the one developed for the Sado bowstring-arch railway bridge, with a highly reliable description of the structure's stiffness, mass, and boundary conditions, as well as its response to environmental and operational actions. Therefore, the online procedure and its performance in detecting early-damage was tested based on a comprehensive dataset of baseline and damaged scenarios simulated using only experimentally obtained actions as input, namely temperature, train loadings and speeds.

In this study, it was found that ARX (30, 30) outperform AR (30) models as feature extractors, by taking advantage of cross information between two sensors (the input and the output). This could be observed when the 30 output ARX parameters showed to be more influenced by EOVs than the 30 input ARX parameters. Although linear, these time series models proved to be sufficiently robust to extract features from responses that result of slightly nonlinear systems, such as the train-bridge system.

The supremacy of the EOVs, which leads to the suppression of the damage influence in the features, was demonstrated. To overcome the challenge of EOV events corrupting the raw data obtained in operational conditions, PCA was successfully applied to the features.

However, the ability to identify early damage, imperceptible in the original signals, while avoiding observable changes induced by variations in train speed or temperature, was only achieved by carefully defining the modelling and fusion sequence of the information. In this sense, a Mahalanobis distance was implemented to provide an additional layer of feature modelling. A performance enhancement was reached by fusing the features from each sensor into a single metric (a distance in the feature space), which displays higher values for distinct structural conditions and nominally null values for identical structural scenarios. This choice allowed the cluster algorithm to effectively separate the features according to the structural conditions observed on site.

Nevertheless, the output of cluster analysis requires user intervention to assess whether clusters are compact or dispersed over time, and therefore it is difficult to apply in automated online SHM. To circumvent this limitation, a moving window procedure comprising 15 trains, based on the average dissimilarity between clusters (DC) and a confidence boundary (CB), was implemented.

To assess whether the proposed procedure was reliable for different damage scenarios, it was applied to a representative set of simulated stiffness reductions (5%, 10% and 20%) in the concrete slab, diaphragm and arches, as well as friction increases in the movements of the bearing devices. This analysis allowed observing that changes as small as 5% of stiffness reduction may be detected in the vast majority of scenarios, using a simple system composed of a few sensors installed on a long-span bridge, while all the remaining severities and friction increments can be detected without false detections. It was also observed that the damage scenarios of the bearing devices are the ones with highest DC values, which leads to the conclusion that the features are most sensitive to

this type of damage. On the other hand, the damages in the concrete (D2) and in the steel-box (D3) present higher DC values when located in the mid-span. In general, damage in the arch (D4) presents higher DC values when located in thirds of the second and third arches. As expected, the lowest severity considered (5% of stiffness reduction) is the most difficult to detect, presenting the lower DC values.

In short, the damage detection strategy has been shown to perform very well on test data with multiple damaged and undamaged states. The procedure requires little user input and updates online. The main disadvantage or limitation that can be pointed out it is not being baseline free. Nevertheless, with the proposed procedure the baseline and the CB can be promptly established during one day for several types of trains with different loads crossing the bridge and increases in robustness as more data are added online. The environmental effects can also be considered since the weather (temperature and wind) varies according to the time of day. After the baseline being built, the detection can be achieved once the first train crosses the bridge after the damage occurrence. Moreover, even with an SHM system not capable of measuring environmental and operational effects, it is possible to successfully detect different types of damage using the bridge's responses to train crossings. This achievement renders the procedure the ability to be less dependent on spatial actions very difficult to characterize, thus contributing for the normalization of SHM procedures. This damage detection strategy also has the advantages of minimizing the number of sensors that need to be installed and, consequently, the cost of the SHM system, as well as allowing for a more automatic and straightforward implementation.

6. Conclusions

This paper presents a comprehensive SHM procedure for conducting continuous online damage detection, using train-induced responses, integrating several algorithms that address detection, EOVs, and online, autonomous classification. The unsupervised machine learning strategy proposed includes the sequential application of ARX models, PCA transformation, and clustering algorithms to the observed data, using a moving window procedure. This strategy also includes an innovative approach to define an adaptive confidence boundary, which can be automatically updated to detect new damage that would progressively occur.

The following conclusions can be drawn from the research work herein presented:

- ARX models showed substantively improved sensitivity when compared with AR models.
- The performed time-series analysis showed to be able of accurately generalize the information present in data, while performing significant compressive fusion.
- The importance of feature modelling was demonstrated, when the effects of EOVs were considerably reduced without the features losing sensitivity to damage.
- EOVs can be more effectively normalized using ARX models rather than AR models.
- Changes as small as 5% of stiffness reduction may be detected in a vast majority of scenarios, with negligible false detection incidences of 2% or less, if the moving window comprises 15 or more trains. Smaller windows lead to larger false detection rates.
- The effectiveness and performance of the proposed procedure for damage detection with a smaller number of sensors than the ones installed on site was also investigated. The results demonstrate that if the number of sensors were reduced from twenty-three to just seven, on a 480 m long bridge, the proposed methodology could be effectively used, but an increase of 5% in false detections would be

observed. Nonetheless, it should be noted that the damage cases that would not be detected are only those with the lowest severity (5% of stiffness reduction).

- Finally, using several train-induced responses from the bridge comprising progressively different types of damage, the effectiveness of an original adaptive CB in detecting new structural changes that may occur in a structure already damaged was successfully demonstrated. Also, the procedure proved to be robust in avowing false damage alerts.

Acknowledgements

This work was financially supported by the Portuguese Foundation for Science and Technology (FCT) through the PhD scholarship SFRH/BD/93201/2013. The authors would like to acknowledge the support of the Portuguese Road and Railway Infrastructure Manager (Infraestruturas de Portugal, I.P), the Portuguese National Laboratory for Civil Engineering (LNEC), the SAFESUSPENSE project - POCI-01-0145-FEDER-031054 (funded by COMPETE2020, POR Lisboa and FCT) and the Base Funding - UIDB/04708/2020 of the CONSTRUCT - Instituto de I&D em Estruturas e Construções - financed by national funds through the FCT/MCTES (PIDDAC).

References

1. Huynh CP, Mustapha S, Runcie P, Porikli F. Multi-class support vector machines for paint condition assessment on the Sydney Harbour Bridge using hyperspectral imaging. *Structural Monitoring and Maintenance* · 2015; **2**(3): 181–197. DOI: 10.12989/smm.2015.2.3.181.
2. Farrar CR, Worden K. *Structural Health Monitoring: a machine learning perspective*. Wiley, pp. 1-45; 2013.
3. Mustapha S, Braytee A, Ye L. Multisource Data Fusion for Classification of Surface Cracks in Steel Pipes. *Journal of Nondestructive Evaluation, Diagnostics and Prognostics of Engineering Systems* 2018; **1**(021007): 1–11. DOI: 10.1115/1.4038862.
4. Saade M, Mustapha S. Assessment of the structural conditions in steel pipeline under various operational conditions – A machine learning approach. *Measurement* 2020; **166**(108262). DOI: 10.1016/j.measurement.2020.108262.
5. Tomé E, Pimentel M, Figueiras J. Damage detection under environmental and operational effects using cointegration analysis – Application to experimental data from a cable-stayed bridge. *Mechanical Systems and Signal Processing* 2020; **135**: 4–8.
6. Cavadas F, Smith IFC, Figueiras J. Damage detection using data-driven methods applied to moving-load responses. *Mechanical Systems and Signal Processing* 2013; **39**(1–2): 409–425. DOI: 10.1016/j.ymssp.2013.02.019.
7. Magalhães F, Cunha A, Caetano E. Vibration based structural health monitoring of an arch bridge : From automated OMA to damage detection. *Mechanical Systems and Signal Processing* 2012; **28**: 212–228. DOI: 10.1016/j.ymssp.2011.06.011.
8. Yan A, Kerschen G, Boe P De, Golinval J. Structural damage diagnosis under varying environmental conditions — Part I : A linear analysis. *Mechanical Systems and Signal Processing* 2005; **19**: 847–864. DOI: 10.1016/j.ymssp.2004.12.002.
9. Alvandi A, Cremona C. Assessment of vibration-based damage identification techniques. *Journal of Sound and Vibration* 2006; **292**: 179–202. DOI: 10.1016/j.jsv.2005.07.036.
10. Meixedo A, Alves V, Ribeiro D, Cury A, Calçada R. Damage identification of a railway bridge based on genetic algorithms. *Maintenance, Monitoring, Safety, Risk and Resilience of Bridges and Bridge Networks - Proceedings of the 8th International Conference on Bridge Maintenance, Safety and Management, IABMAS 2016*, Foz Do Iguaçu; Brazil: 2016.
11. Neves AC, GonzaLez I, Karoumi R, Leander J. The influence of frequency content on the performance of artificial neural network – based damage detection systems tested on numerical and experimental bridge data. *Structural Health Monitoring* 2020; **I**–**17**. DOI: 10.1177/1475921720924320.
12. Santos JP, Crémona C, Calado L, Silveira P, Orcesi AD. On-line unsupervised detection of early damage. *Structural Control and Health Monitoring* 2015. DOI: 10.1002/stc.
13. Santos JP, Crémona C, Orcesi AD, Silveira P. Multivariate statistical analysis for early damage detection. *Engineering Structures* 2013; **56**: 273–285. DOI: 10.1016/j.engstruct.2013.05.022.
14. Entezami A, Shariatmadar H, Mariani S. Fast unsupervised learning methods for structural health monitoring with large vibration data from dense sensor networks. *Structural Health Monitoring* 2019; **I**–**26**. DOI: 10.1177/1475921719894186.
15. Nie Z, Lin J, Li J, Hao H, Ma H. Bridge condition monitoring under moving loads using two sensor measurements. *Structural Health Monitoring* 2019: 1–21. DOI: 10.1177/1475921719868930.
16. Azim R, Gül M. Damage detection of steel girder railway bridges utilizing operational vibration response. *Structural Control and Health Monitoring* 2019(August): 1–15. DOI: 10.1002/stc.2447.

17. Gonzalez I, Karoumi R. BWIM aided damage detection in bridges using machine learning. *Journal of Civil Structural Health Monitoring* 2015; **5**(5): 715–725. DOI: 10.1007/s13349-015-0137-4.

18. Neves AC, González I, Leander J, Karoumi R. Structural health monitoring of bridges : a model-free ANN-based approach to damage detection. *Journal of Civil Structural Health Monitoring* 2017(7): 689–702. DOI: 10.1007/s13349-017-0252-5.

19. Nie Z, Guo E, Li J, Hao H, Ma H, Jiang H. Bridge condition monitoring using fixed moving principal component analysis. *Structural Control and Health Monitoring* 2020(February): 1–29. DOI: 10.1002/stc.2535.

20. Meixedo A, Santos J, Ribeiro D, Calçada R, Todd M. Damage detection in railway bridges using traffic-induced dynamic responses. *Engineering Structures* 2021; **238**(112189). DOI: 10.1016/j.engstruct.2021.112189.

21. ANSYS. Academic Research. Release 17.1 2016.

22. REFER. Variante de Alcácer 2010.

23. Albuquerque C, Silva ALL, Jesus AMP De, Calçada R. An efficient methodology for fatigue damage assessment of bridge details using modal superposition of stress intensity factors. *International Journal of Fatigue* 2015; **81**: 61–77. DOI: 10.1016/j.ijfatigue.2015.07.002.

24. A. Meixedo, A. Gonçalves, R. Calcada, J. Gabriel, H. Fonseca RM. Weighing in motion and wheel defect detection of rolling stock. *exp.at 2015 - 3rd Experiment International Conference: Online Experimentation*, University of Azores, Ponta Delgada, Sao Miguel, Azores Island: ISBN: 978 146737717-1; 2015.

25. Min X, Santos L. *Ensaios dinâmicos da ponte ferroviária sobre o rio sado na variante de alcácer*. Lisboa [Portuguese]: 2011.

26. Ribeiro D, Calçada R, Delgado R, Brehm M, Zabel V. Finite element model updating of a bowstring-arch railway bridge based on experimental modal parameters. *Engineering Structures* 2012; **40**: 413–435. DOI: 10.1016/j.engstruct.2012.03.013.

27. Meixedo A, Ribeiro D, Santos J, Calçada R, Todd M. Progressive numerical model validation of a bowstring-arch railway bridge based on a structural health monitoring system. *Journal of Civil Structural Health Monitoring* 2021; **11**(2): 421–449. DOI: 10.1007/s13349-020-00461-w.

28. Pimentel R, Ribeiro D, Matos L, Mosleh A, Calçada R. Bridge Weigh-in-Motion system for the identification of train loads using fiber-optic technology. *Structures* 2021; **30**(November 2020): 1056–1070. DOI: 10.1016/j.istruc.2021.01.070.

29. Santos J. Smart Structural Health Monitoring Techniques for Novelty Identification in Civil Engineering Structures. PhD Thesis. Instituto Superior Técnico - University of Lisbon, 2014.

30. Wardhana K, Hadipriono FC, Asce F. Analysis of Recent Bridge Failures in the United States. *Journal of Performance of Constructed Facilities* 2003; **17**(3): 144–150.

31. Akesson B. *Understanding Bridge Collapses*. 1st ed. London, UK: Taylor & Francis; pp; 2008.

32. Mohiuddin A. Khan. *Bridge and Highway. Structure Rehabilitation and Repair*. 1st ed. New York, USA: McGraw-Hill, pp. 53-59; 2010.

33. Box G, Jenkins G, Reinsel G, Ljung G. *Time Series Analysis: Forecasting and Control*. Fifth Edit. Englewood Cliffs, NJ: Wiley, pp. 509-524; 2016.

34. Ribeiro D, Leite J, Meixedo A, Pinto N, Calçada R, Todd M. Statistical methodologies for removing the operational effects from the dynamic responses of a high-rise telecommunications tower. *Structural Control and Health Monitoring* 2021; **28**(4): e2700. DOI: 10.1002/stc.2700.

35. Hu WH, Moutinho C, Caetano E, Magalhes F, Cunha L. Continuous dynamic monitoring of a lively footbridge for serviceability assessment and damage detection. *Mechanical Systems and Signal Processing* 2012; **33**: 38–55. DOI: 10.1016/j.ymssp.2012.05.012.

36. Tomé ES, Pimentel M, Figueiras J. Online early damage detection and localisation using multivariate data analysis : Application to a cable - stayed bridge. *Structural Control Health Monitoring* 2019(July): 1–20. DOI: 10.1002/stc.2434.

37. Härdle WK, Simar L. *Applied Multivariate Statistical Analysis*. 4th ed. Springer, pp. 215-247; 2015.

38. Jolliffe IT. Principal Component Analysis. 2nd ed., New York: Springer, pp. 112-147; 2002.

39. Rendón E, Abundez I, Arizmendi A, Quiroz EM. Internal versus External cluster validation indexes. *International Journal of Computers and Communications* 2011; **5**(1).

40. Cury A, Cremona C. Novelty detection based on symbolic data analysis applied to structural health monitoring. *Bridge Maintenance, Safety and Management - IABMAS'10* 2010: 172–182.

41. Marian Ralbovsky, Santos JP, Kwapisz M, Dallinger S, Catarino J. Damage detection based on structural response to Temperature changes and model updating. *EWSHM - European Workshop of Structural Health Monitoring*, Nantes, France: 2014.

42. Hastie T, Tibshirani R, Friedman J. *The Elements of Statistical Learning, Data Miningm Inference, and Prediction*. 2nd ed. Stanford, USA: Springer, pp. 460-462; 2011.

43. Santos J, Crémona C, Calado L. Real-time damage detection based on pattern recognition. *Structural Concrete 17* 2016; **17**(3): 338–354. DOI: 10.1002/suco.201500092.

44. Posenato D, Kripakaran P, Smith IFC. Methodologies for model-free data interpretation of civil engineering structures. *Computers & Structures* 2010; **88(7-8)**: 467–482. DOI: 10.1016/j.compstruc.2010.01.001.

45. Glaser SD, Tolman A. Sense of Sensing: From Data to Informed Decisions for the Built Environment. *Journal of Infrastructure Systems* 2008; **14**(1): 4–14. DOI: 10.1061/(ASCE)1076-0342(2008)14:1(4).

46. Worden K, Sohn H, Farrar CR. Novelty detection in a changing environment: regression and interpolation approaches. *Journal*

of Sound and Vibration 2002; **258**(4): 741–761. DOI: 10.1006/jsvi.2002.5148.

47. Datteo A, Busca G, Quattromani G, Cigada A. On the use of AR models for SHM: A global sensitivity and uncertainty analysis framework. *Reliability Engineering and System Safety* 2018; **170**: 99–115. DOI: 10.1016/j.ress.2017.10.017.